Drivers of Air-Sea CO_2 Flux Seasonality and its Long-Term Changes in the NASA-GISS model CMIP6 submission.

Paul Lerner[1], Anastasia Romanou[1,2], Maxwell Kelley[1,3], Joy Romanski[1,4], Reto Ruedy[1,3], Gary Russell[1]

[1]NASA-GISS, New York City, NY, USA
[2]Applied Physics and Applied Math, Columbia University, New York City, NY, USA
[3]SciSpace LLC, New York City, NY, USA
[4]Center for Climate Systems Research, Columbia University, New York City, NY, USA

Key Points:

- The seasonality of the CO_2 flux, pCO_2, and their drivers in the NASA-GISS model E2.1-G are evaluated using a suite of monthly climatologies
- The seasonal cycles of the CO_2 flux and $pCO_{2,sw}$ are temperature-driven in the subtropics and DIC-driven in the Southern Ocean
- In an idealized future forcing scenario, changes in the flux are largely driven by changes in the sensitivity of pCO_2 to its drivers

Corresponding author: Paul Lerner, paul.lerner@nasa.gov

Abstract

Climate change will affect both the mean state and seasonality of marine physical and biogeochemical properties, with important implications for the oceanic sink of atmospheric CO_2. Here, we investigate the seasonal cycle of the air-sea exchange of CO_2 and $pCO_{2,sw}$ (surface seawater pCO_2) and their long term changes using the CMIP6 submission of the NASA-GISS modelE (GISS-E2.1-G). In comparison to the CMIP5 submission (GISS-E2-R), we find that on the global scale, the seasonal cycles of the CO_2 flux and NPP have improved, while the seasonal cycles of DIC, alkalinity, and macronutrients have deteriorated. Moreover, for all ocean biogeochemietry fields, changes in skill between E2.1-G and E2-R display large regional variability. For E2.1-G, we find similar modeled and observed CO_2 flux seasonal cycles in the subtropical gyres, where seasonal anomalies of $pCO_{2,sw}$ and the flux are temperature-driven, and the Southern Ocean, where anomalies are DIC-driven. Biases in these seasonal cycles are largest in the subpolar and equatorial regions, driven by a combination of biases in temperature, DIC, alkalinity, and wind speed.

When comparing the historical simulation to a simulation with an idealized increase in atmospheric pCO_2, we find that the seasonal amplitudes of the CO_2 flux and $pCO_{2,sw}$ generally increase. These changes are produced by increases in the sensitivity of $pCO_{2,sw}$ to its respective drivers. These findings are consistent with the notion that the seasonality of $pCO_{2,sw}$ is expected to increase due to the increase of atmospheric pCO_2, with changes in the seasonality of temperature, DIC, and alkalinity having secondary influences.

Plain Language Summary

The ocean plays an important role in removing human CO_2 emissions from the atmosphere. The removal varies seasonally, and this variability is expected to change as the ocean's carbon content increases. To predict these changes, models need to accurately simulate seasonal changes of the air-sea exchange of CO_2. In this study, we examine the seasonal cycle of the air-sea exchange of CO_2 in the CMIP6 version of the NASA-GISS modelE (GISS-E2.1-G). We find good agreement between the seasonal cycles in the model and observations in the subtropical latitudes, where seasonal changes are mainly caused by temperature changes, and in the Southern Ocean, where seasonal changes are mainly caused by changes in dissolved inorganic carbon. Agreement is much poorer in high latitudes and tropical waters, where discrepancies in model wind speed, temperature, dissolved inorganic carbon, and alkalinity all contribute to differences between the modeled and observed seasonal cycle of air-sea CO_2 exchange. We further find, under future atmospheric CO_2 increase, that seasonal extremes in the air-sea exchange of CO_2 increase in most of the

ocean. Our findings support the idea that, under increased CO_2 levels, the change in the ocean's ability to take CO_2 from the atmosphere will be seasonally dependent.

1 Introduction

Roughly one-third of the carbon emitted to the atmosphere by human activity since the industrial revolution has been absorbed by the ocean, as a result of a rise in atmospheric pCO_2 by ~120 μatm (Le Quéré et al., 2018). The rise in atmospheric pCO_2 has already impacted ocean ecosystems in a variety of ways, including increasing ocean acidification to the potential detriment of calcareous organisms, increasing metabolic rates of marine organisms via increasing temperature, and increasing stratification and changing circulation patterns, resulting in profound shifts in the species distribution in the ocean (Doney et al., 2012). These impacts are expected to only strengthen as anthropogenic climate change is projected to further increase sea surface temperatures, reduce pH, and reduce ocean net primary productivity through the end of the 21st century (Bopp et al., 2013).

Previous modeling efforts have shown that in response to increasing atmospheric and oceanic pCO_2, the seasonality (i.e., the seasonal amplitude, or the difference between the maximum and minimum values within a seasonal cycle) of sea surface pCO_2 will also increase (Rodgers et al., 2008; Gorgues et al., 2010; Gallego et al., 2018). These modeling studies have been supported by a recent paper showing that the seasonal cycle of pCO_2 has increased in response to the increase in annual mean pCO_2 between 1985 and 2014 (Landschützer et al., 2018). The seasonal amplitude of surface ocean pCO_2 is primarily controlled by temperature, alkalinity, and DIC (Takahashi et al., 2002; Sarmiento & Gruber, 2006). When the seasonal cycle of surface ocean pCO_2 is examined, it is often split into its thermally driven and non-thermally (DIC+alkalinity) driven components (Sarmiento & Gruber, 2006; Landschützer et al., 2014; Fay & McKinley, 2017; Landschützer et al., 2018). These components often act in opposing directions. For example, in the subtropical gyres of the ocean, the summertime increase in thermally driven pCO_2 is somewhat counteracted by the decrease in pCO_2 due to increased stratification bringing less DIC to the surface, although the thermal effect dominates (Takahashi et al., 2002; Fay & McKinley, 2017). In the subpolar regions, the opposite situation occurs, with the wintertime mixing driving an increase in non-thermal pCO_2 that is somewhat, but not completely, counteracted by the decrease in temperature driving a decrease in thermal pCO_2. Calculations using only the carbonate system and assuming equilibrium between atmospheric and ocean pCO_2 show that under a scenario of increasing atmospheric CO_2 concentration, there is amplification of both thermal and non-thermal seasonal forcing of pCO_2 (Riebesell et al., 2009). Observational evidence suggests that drivers of increases in the seasonality of pCO_2 are regionally dependent. In the subtropical gyres, an increase in the seasonality of pCO_2 is driven by an increase in the seasonality of its thermally-driven component. On the other hand, in the subpolar regions and Southern ocean, the increase in the seasonality of pCO_2 is driven by the

increase in the seasonality of its non-thermally driven component (Landschützer et al., 2018). However, the previous generation of Coupled Model Intercomparison Project version 5 (CMIP5) models showed that the increase in the seasonality of pCO_2 is driven more by temperature than DIC in all regions except the Southern Ocean (Gallego et al., 2018). These previous studies motivate two important questions regarding the new generation of CMIP6 models: (1) how well do these models capture the seasonality of the CO_2 flux and surface ocean pCO_2, and (2) what drives future changes in the seasonality of the CO_2 flux and surface ocean pCO_2 in these models? Addressing these questions rigorously requires a detailed investigation into the seasonal cycle of ocean carbon uptake, as well as its biases. Thus, the primary goal of this study is to document the NASA-GISS CMIP6 ocean carbon cycle simulation, with a focus on understanding the biases and changes in the seasonal cycle of ocean carbon uptake and pCO_2.

In this study, we compare the modeled and observed time-averaged seasonal cycles of the CO_2 flux and ΔpCO_2 (the difference between surface ocean and atmospheric pCO_2), and determine how the seasonality of these CO_2 fields changes after 70 yrs of linearly increasing atmospheric CO_2 by 1% annually, at the time of a doubling of atmospheric CO_2 from the pre-industrial level. First, we provide an overview of the simulated and observed CO_2 flux, and also compare model and observed surface properties that can influence the bias in the flux (section 3.1.1). We also briefly evaluate how these model biases have changed from the CMIP5 submission of the NASA-GISS model E2-R (section 3.1.2). In sections comparing the CMIP5 to CMIP6 submissions, we refer to the CMIP5 incarnation of the model as E2-R and CMIP6 incarnation as E2.1-G. We then compare simulated (by E2.1-G) and observed seasonal cycles of the CO_2 flux, ΔpCO_2, and sea surface properties that can drive these fields (section 3.2.1). The averaging period for the model is near the end of the historical period, and is always aligned to the temporal coverage of every dataset against which the model is compared. As with the annual climatologies, the ability of model E2.1-G to capture these seasonal cycles is compared to that of E2-R (section 3.2.2).

In our analysis, we tease apart the drivers of the seasonal cycles of the CO_2 flux and surface ocean pCO_2 in both model E2.1-G and observations (section 3.2.3-3.2.4). We then difference the model means and seasonal amplitudes between the end of the historical period (1995-2014) and from the simulation in which atmospheric CO_2 increases by 1% annually after reaching twice the pre-industrial level (1910-1930; section 3.3.1). We refer to these differences as long term changes in ΔpCO_2 and the CO_2 flux. Finally, the major drivers of changes in the seasonal cycle of the CO_2 flux are assessed in both model and observations (section 3.3.2). Our analysis closely examines the seasonal cycle of sea surface properties in nine major ocean basins: the subpolar North Atlantic, the subtropical

North Atlantic, the equatorial Atlantic, the subtropical South Atlantic, the subpolar North Pacific, the subtropical North Pacific, the equatorial Pacific, the subtropical South Pacific, and the Southern Ocean. The difference between the seasonal cycles and their drivers are discussed in section 4. Conclusions follow in section 5.

2 Methods

2.1 Model

The characteristics of the physical ocean component of the GISS GCM (GISS-E2.1-G) are described more fully in Kelley et al. (2020). Since the CMIP5 incarnation of GISS-E2-R (Schmidt et al., 2014; Romanou et al., 2013), key updates have included finer upper-ocean layering, improved implementation of mesoscale eddy transport, 3D variation of mesoscale diffusivity, a higher-order advection scheme, vertical mixing driven by tidal dissipation, increased ventilation of marginal seas, and a scheme for accelerated tracer transport. As in E2-R, mass-conserving numerics and surface-flux formulations ensure consistent treatment of biogeochemical (BGC) constituents under riverine inputs, sea ice formation/melt, evaporation-precipitation, and all other model processes (Ito et al., 2020). The horizontal resolution is 1×1.25 degrees in latitude and longitude respectively, and the vertical resolution is 40 quasi-constant pressure layers. Ocean only simulations of passive tracer uptake (CFC) showed good agreement with observations (Romanou et al., 2017).

The ocean carbon cycle module is an update of the one used in E2-R (Romanou et al., 2013, 2014) and which originated from the NASA Ocean Biogeochemistry Model (NOBM; Gregg and Casey (2007)). It includes 4 phytoplankton species (diatoms, chlorophytes, cyanobacteria and coccolithophores), four nutrient species (nitrate, silicate, ammonia and iron), three detrital pools (nitrate/carbon, silicate and iron) and one heterotroph species. Carbon cycling is represented through dissolved organic (DOC) and dissolved inorganic carbon (DIC) and interacts with atmospheric CO_2 through gas exchange parameterization, following the CMIP6 protocol (Orr et al., 2017). Light profiles from the atmospheric radiation module are propagated underwater into the ocean and spectrally decomposed to 33 wavebands that are used to compute growth of the phytoplankton groups, sinking profiles, as well as changes in the vertical distribution of ocean temperatures due to biologically mediated absorption and scattering in the water column (Gregg & Conkright, 2002). Latto and Romanou (2018) showed that ocean carbon states estimated from the GISS E2.1-G model with the E2-R carbon cycle agreed well with observations in most regions, and that study led to the current improvements in the carbon cycle simulations.

Latest improvements to the ocean carbon cycle model include the introduction of exponential profiles for the diatom sinking and the detritus settling. A prognostic alkalinity scheme has been implemented following OCMIP2 parameterization in order to better simulate carbonate chemistry and the oceanic carbonate pump. Atmospheric dust deposition is now interactive and consistent with the model climate, and thus the ocean iron cycle is forced from the historical annual cycle climatology extracted from the GISS E2.1-G online dust simulations which include eight externally mixed minerals (illite, kaolinite, smectite, carbonates, quartz, feldspar, iron oxides and gypsum) plus internal mixtures between seven minerals and iron oxides (Perlwitz & Pérez García-Pando, 2015; Perlwitz et al., 2015). The masses of free and structural iron and their fractions of total iron have been evaluated using measurements from Izaña Observatory (Pérez García-Pando et al., 2016). Riverine delivery of BGC constituents is also recently implemented and coupled to the prognostic river runoff calculated in GISS E2.1-G as part of the simulated global hydrological cycle. The concentrations of DOC, DIC, nitrate, silicate and Fe at all the major and many minor river mouths are obtained from an annual climatology (Da Cunha et al., 2007) and they modulate the biogeochemical characteristics of the freshwater outflow into the ocean at these sites. The riverine contribution to alkalinity is neglected in the model.

2.2 Observations

We use a suite of observationally based climatologies to evaluate output from the historical simulation, each of which are interpolated onto the ocean model grid prior to comparison. The monthly climatolgies used in this study include those for ΔpCO_2, the CO_2 flux, dissolved inorganic carbon (DIC), alkalinity, macronutrients (nitrate and silicate), net primary production (NPP), temperature, salinity, mixed layer depth, and surface wind speed. The pCO_2 and the air-sea CO_2 flux are evaluated against the climatologies of Landschützer et al. (2014), which use a neural-networking approach to map ΔpCO_2 and CO_2 flux observations from the Surface Ocean Carbon Atlas, version 2 (SOCATv2) to a gridded product with a $1^\circ \times 1^\circ$ horizontal resolution. DIC and alkalinity are obtained from the surface ocean climatology of Takahashi et al. (2014). In this climatology, DIC is derived by using an inorganic carbon chemistry model that uses as inputs climatological distributions of pCO_2, total alkalinity, salinity, and temperature. These authors obtained distributions of salinity and temperature from the World Ocean Atlas, 2009 climatology, and sea surface pCO_2 using the methodology of Takahashi et al. (2009) updated to use 2005 as the reference year. The methodology of Takahashi et al. (2009) interpolates sea surface pCO_2 from the LDEO database onto a $4^\circ \times 5^\circ$ ocean grid using an interpolation method based on a 2-d advection-diffusion equation. They further derived alkalinity using a linear relationship between alkalinity and salinity from 24 different oceanic regions, and tested their salinity-

derived alkalinity and model-derived DIC values against measurements from the GLODAP database (Key et al., 2004), the CARINA program (Key et al., 2010), and measurements from the LDEO database. They found that the calculated values were consistent with the measured values within their respective measurement uncertainties. The data provided in this climatology are referenced to year 2005. Note that, while more recent climatologies of DIC and alkalinity are available from GLODAPv2 (Key et al., 2015; Lauvset et al., 2016), to our knowledge these datasets are only available as annual climatologies, not monthly climatologies which were necessary for this study.

Macronutrients are evaluated against climatologies of nitrate and silicate from the World Ocean Atlas, 2013 (Garcia et al., 2014). Net primary production is obtained from the Carbon-based production model, version 2 (Westberry et al., 2008). The CbPMv2 relates NPP to the product of phytoplankton carbon concentration, as estimated by remote sensing retrievals of particulate backscattering coefficients, and phytoplankton growth rates, as estimated from carbon-to-chlorophyll ratios. Here, we use NPP estimates provided by the Ocean Productivity repository: `http://www.science.oregonstate.edu/ocean.productivity/index.php` (Westberry et al., 2008), calculated based on optical properties retrieved from SeaWiFS measurements between 1998 and 2007.

Temperature and salinity are evaluated against the Roemmich-Gilson ARGO climatology derived from ARGO floats deployed between 2004 and 2012 (Roemmich & Gilson, 2009). The mixed layer depth is also evaluated against an ARGO-based climatology, in which vertical density differences obtained from ARGO floats deployed between 2000 and 2016 are used to determine the depth of the mixed layer (Holte et al., 2017). Finally, surface wind speed is obtained from the second Modern-Era Retrospective analysis for Research and Applications (MERRA2), a NASA atmospheric reanalysis that begins in 1980, and includes monthly gridded values with a horizontal resolution of $0.625^\circ \times 0.5^\circ$ (Bosilovich et al., 2015). In comparing to the model, we take the average of the reanalysis fields each month between 2004 and 2012.

To evaluate model skill in capturing the CO_2 flux, pCO_2, and other sea surface properties that impact these CO_2 fields, we calculated the normalized root-mean square error and bias for the global surface ocean. The normalized root mean square is: NRMSE= $\sqrt{\frac{\sum_i (x_{m,i}-x_{o,i})^2}{N}}/\overline{x}_o$, where x is a sea surface property, i is an index for ocean surface grid cells where model values and observations are available, m stands for model, o stands for observations, and N is the number of available coinciding model values and observations, and $\overline{x_o}$ is the mean of x over the surface ocean. The bias is: bias= $\frac{\sum_i (x_{m,i}-x_{o,i})}{N}$. For evaluating NRMSE and the bias, the annual, as opposed to monthly, climatologies are used.

Table 1. Periods over which the historical run is averaged when compared to observations

dataset	averaging period	reference
CO_2 flux/ΔpCO_2 climatology	1998-2011	Landschützer et al. (2014)
DIC/Alk climatology	2000-2010	Takahashi et al. (2014)
ARGO T/S climatology	2004-2012*	Roemmich and Gilson (2009)
CbPMv2 NPP	1997-2008	Westberry et al. (2008)
MLD climatology	2000-2016*	Holte et al. (2017)
WOA2013 Nitrate and Silicate	1960-2010	Garcia et al. (2014)
MERRAv2 wind speed	2004-2012*	Bosilovich et al. (2015)

*For comparisons to E2-R, climatologies range from the same start-year to the end year 2010.

2.3 Experiments

We analyze results from NASA-GISS-E2.1-G simulations for the historical period, forced with observed forcing, and an idealized future forcing scenario in which the atmospheric concentration of CO_2, starting from the pre-industrial CO_2 concentration in 1850, increases by 1% annually until it reaches double the pre-industrial value (around year 70 of the simulation). For convenience, we refer to the latter scenario as the 1% simulation. For the historical period, model output is averaged over the same period that is represented by the corresponding dataset (Table 1). For example, when comparing to the climatology of Landschützer et al. (2014), which includes the monthly averaged CO_2 flux and ΔpCO_2 between 1998 and 2011, we take the model's monthly average CO_2 flux and pCO_2 fields over the same period. In this way, we attempt to limit model-data bias that may be due to differences in the timing of sampling of model output vs. timing of sampling of observations. However, we note that when the averaging period is shorter than 20 yrs, some of the discrepancy between the model and the observed change might be attributed to internal variability. For the idealized 1% simulation, we take a 20 year average with the year in which the atmospheric CO_2 concentration reaches 2× its pre-industrial value as the central value. Model spin ups were carried out for 700 years off an equilibrated simulation of the pre-industrial ocean-atmosphere-ice system with prognostic CO_2 and about 500 years of accelerated DIC, and then the carbon cycle was again simulated online for another 100 years, for a total of ~1300 years.

In addition to the time-averaging, the model and observational fields are also either regionally weighted-averaged (for ΔpCO_2, MLD, DIC, alkalinity, nitrate, and silicate), or regionally integrated (for CO_2 flux and net primary production). We ensure that for each property, only grid-cells that contain both simulated and observed values are included in the regional average or regional integration. For the weighted averages, properties with con-

centration units are weighted by the mass of water in the model grid cell (ΔpCO_2, DIC, alkalinity, nitrate, and silicate), and MLD is weighted by the surface area of the model grid cell. The regionally integrated fields (CO_2 flux and net primary production) are further normalized by the number of grid cells in the region for which both modeled and observed values exist, so that regionally-averaged carbon fluxes (in Pg C/yr) are calculated. The regions considered are the subpolar North Atlantic (45°N to 60°N, 75°W to 0°E), the subtropical North Atlantic (15°N to 45°N, 75°W to 0°E), the equatorial Atlantic (15°S to 15°N, 75°W to 0°E), the subtropical South Atlantic (60°S to 45°S, 75°W to 15°E), the subpolar North Pacific (45°N to 60°N, 140°E to 65°W), the subtropical North Pacific (140°E to 110°W), the equatorial Pacific (15°S to 15°N, 150°E to 75°W), the subtropical South Pacific (45°S to 15°S, 150°E to 75°W), and the Southern Ocean (60°S to 45°S, 180°E to 180°W). While not encompassing the entire ocean, the regions are meant to represent either major basins which are important carbon sinks (e.g., the North Atlantic and the Southern Ocean), or areas of the largest biases in the CO_2 flux (e.g., the subpolar regions and the equatorial Pacific). So that our examination of the seasonality of the flux and pCO_2 is not influenced by seasonal sea ice, we only consider latitudes equatorward of 60°N and 60°S. We also remove all remaining grid cells that include seasonal sea ice from the regional averages. Our motivation for being restricted to ice-free waters is two-fold. First, in our analysis of the drivers (section 3.2.3-3.2.4), we do not consider the influence of changes in sea ice coverage on the air-sea flux, being mainly interested in the biogeochemical and thermal drivers of the seasonality of the CO_2 flux and ΔpCO_2. Second, the model's diagnostic $pCO_{2,sw}$ output was erroneously scaled by a factor of (1 - (% sea ice cover)). This error caused the model's diagnostic for $pCO_{2,sw}$ to be much lower than expected in regions of seasonal sea ice.

Finally, when discussing seasonality in specific regions, "boreal" will be used to specify northern hemisphere and equatorial winter (Dec,Jan,Feb), spring (Mar,Apr,May), summer (Jun,Jul,Aug), and fall (Sep,Oct,Nov). Likewise, "austral" will be used to specify southern hemisphere winter (Jun,Jul,Aug), spring (Sep,Oct,Nov), summer (Dec,Jan,Feb), and fall (Mar,Apr,May). Seasons will not be specified as "boreal" or "austral" when referring to regions in both hemispheres.

3 Results

3.1 Annual Climatologies

3.1.1 Comparison to Observations

We find that $pCO_{2,sw}$ shows better agreement with observations in the subptroical regions and Southern Ocean than in the equatorial and subpolar regions (Fig. 1a). In the subtropical and Southern Ocean regions, the model shows a difference that amounts to $\sim \pm 5\%$ of the observed $pCO_{2,sw}$, while the difference is $\sim \pm 25\%$ of the observed $pCO_{2,sw}$ in the equatorial Pacific, subpolar North Atlantic, and subpolar North Pacific. In the subtropical regions, the positive pCO_2 bias is consistent with the positive temperature biases, since the higher model temperature decreases the solubility of pCO_2 in seawater. The bias in $pCO_{2,sw}$ is also consistent with the negative NPP bias, which causes the model to draw down less DIC than in observations and hence increases the DIC available to be converted to pCO_2.

In the subpolar gyres and Southern Ocean, model $pCO_{2,sw}$ is generally less than observed (by ~25% in the subpolar regions, and ~5% in the Southern Ocean; Fig. 1a). In the subpolar North Pacific, the negative temperature bias partly contributes to the negative bias in pCO_2, with higher solubility driving pCO_2 downward in the model compared to observations (Fig. 1f). The large bias in the mixed layer depth in the subpolar North Atlantic (Fig. 1d) largely contributes to the pCO_2 bias. This is because while there is a positive bias in alkalinity and DIC throughout the water column in this region, the model only underestimates the vertical gradient in DIC (Fig. S1,S2). Thus the increase in surface DIC in the model due to wintertime mixing is less than that in observations, leading to a more negative difference between DIC and alkalinity in the model than in observations. Since DIC and alkalinity have opposing effects on $pCO_{2,sw}$, with DIC increasing $pCO_{2,sw}$ and alkalinity decreasing $pCO_{2,sw}$, the smaller difference between DIC and alkalinity in the model leads to negative bias in $pCO_{2,sw}$ in this region. While the Southern Ocean does not exhibit the negative temperature bias in the northern subpolar regions, it does exhibit a positive NPP bias (Fig. 1e) and negative DIC bias, suggesting the larger than observed productivity is leading to enhanced DIC drawdown and reduced $pCO_{2,sw}$.

Like the subtropical regions, the equatorial Atlantic exhibits a positive $pCO_{2,sw}$ bias (~20%) that appears associated with a positive temperature bias (Fig. 1a,f). On the other hand, in the equatorial Pacific, there is a negative bias in $pCO_{2,sw}$ (~25%) that appears associated with a positive bias in NPP (Fig. 1e) and temperature (Fig. 1f). In particular, the region of large $pCO_{2,sw}$ bias in the model off the coast of Peru is associated with the region in the equatorial Pacific where the NPP and SST biases are largest (Fig. 1e,f), sug-

gesting that the reason for the discrepancy between the observed and model $pCO_{2,sw}$ in this region is a combination of the model's overestimation of productivity and underestimation of DIC upwelled from waters below the thermocline.

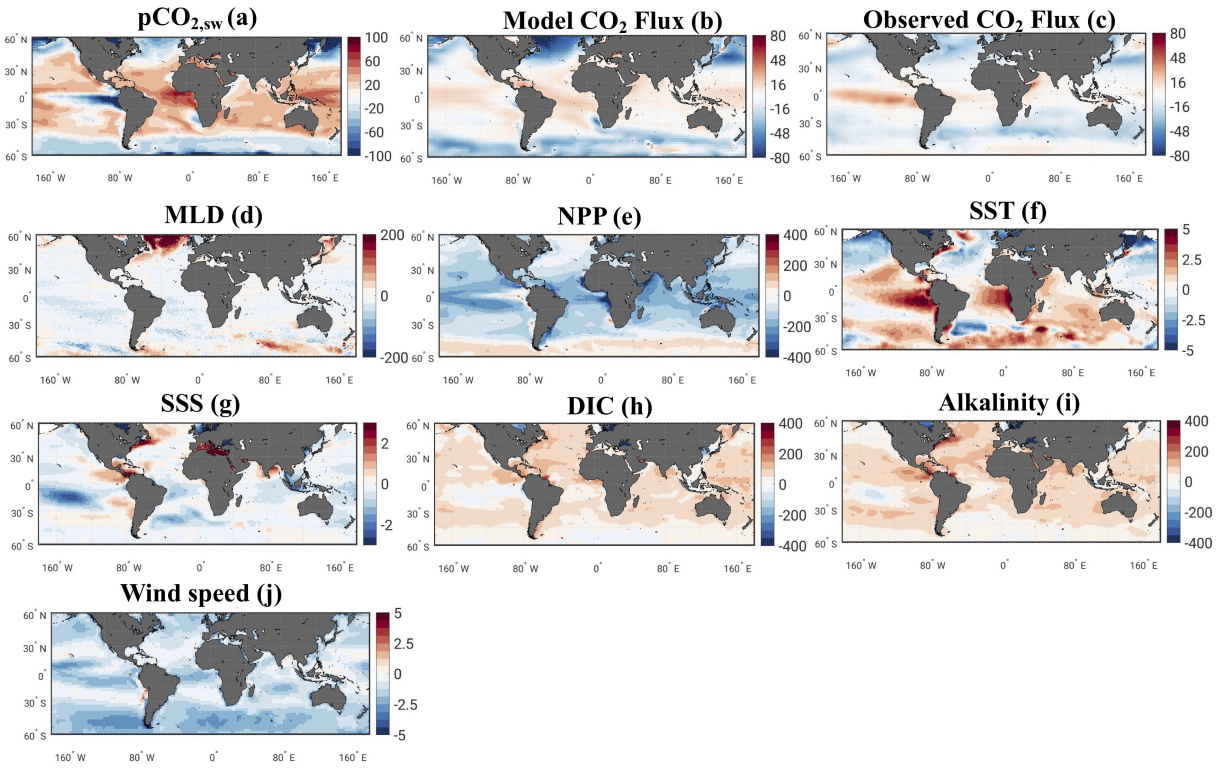

Figure 1. The first panel (a) shows biases in $pCO_{2,sw}$ (μatm) between the model and the annual climatology of Landschützer et al. (2014). The next two panels show the air-sea flux of CO_2 (g C/m^2/yr) from (b) the model and (c) from the annual climatology of Landschützer et al. (2014). Positive values represent outgassing. The remaining panels show biases in (d) the mixed layer depth (m), (e) net primary production (g C/m^2/yr), (f) sea surface temperature (°C), (g) sea surface salinity (psu), (h) sea surface dissolved inorganic carbon (μmol/kg), (i) sea surface alkalinity (meq/kg), (j) surface wind speed (m/s). We do not show fields to the south and north of 60°S and 60°N, respectively, due to an incorrect scaling of the model's diagnostic pCO_2 output by the fraction of sea-ice free water.

Turning to the CO_2 flux, the largest biases are in the equatorial Pacific, where the model has weak outgassing compared to observations, and in the subpolar North Atlantic and the Southern Ocean, where CO_2 uptake in the model is too large compared to observations. The model also underestimates the CO_2 flux in the subtropical gyres (North and South Atlantic, North and South Pacific) and overestimates the outgassing in the equatorial Atlantic. Additionally, there are a few local discrepancies between the direction of CO_2 gas exchange. Along the Peruvian margin, observations show outgassing of CO_2, while the model simulates strong uptake and, in the Southern Ocean south of 60°S, observations show either no net flux or slight outgassing of CO_2, while the model shows strong uptake.

The biases in $pCO_{2,sw}$ should at least in part control the biases in the CO_2 flux, as the air-sea exchange of CO_2 is partly a function of the air-sea gradient in pCO_2. The relationship between the CO_2 flux (F_{CO2}) and ΔpCO_2 follows:

$$F_{CO2} = k(Ws,T)\alpha(T,S)\Delta pCO_2(1-sice), \quad (1)$$

where $k(T,Ws)$, $\alpha(T,S)$, T, S, Ws, and $sice$ are the piston velocity, the solubility of CO_2, temperature, salinity, the surface wind speed, and fractional sea ice coverage, respectively. Biases in any one or a combination of the above factors, along with the air-sea gradient in pCO_2, may contribute to the biases in the CO_2 flux. To determine the extent to which the biases in the CO_2 flux are related to the biases in $pCO_{2,sw}$, we provide scatterplots of the two CO_2 fields in each region (Fig. S3). We find a significant positive relationship between the biases in $pCO_{2,sw}$ and the biases in the CO_2 flux in most regions. The one exception is the equatorial Atlantic, where biases in wind speed may be just as important in controlling the flux (see section 3.2.4). The close relationship between the CO_2 flux and $pCO_{2,sw}$ biases also explains the reversal in sign of the CO_2 flux near the Peruvian margin and Southern Ocean compared to observations. In both of these regions, the positive biases in NPP increase the drawdown of DIC, decreasing $pCO_{2,sw}$. Furthermore, underway measurements of $pCO_{2,sw}$ suggest that high $pCO_{2,sw}$ values are associate with cold, nutrient-rich, and oxygen depleted upwelled waters (Copin-Montégut & Raimbault, 1994; Boutin et al., 1999). This is because upwelled waters, particularly from low-oxygen waters that have been subject to intensive remineralization, are enriched in DIC, and their vertical transport to the surface increases $pCO_{2,sw}$ (Feely et al., 2006; Takahashi et al., 2009; Sutton et al., 2014). In the Southern Ocean, wintertime upwelling in the Antarctic Divergence zone has a similar effect; bringing DIC-enriched waters to the surface to increase $pCO_{2,sw}$ (Lovenduski et al., 2007; Gruber et al., 2019). Since the positive biases in temperature in both regions suggest reduced upwelling along the Peruvian margin and Southern Ocean, the reduction of both processes may serve to further increase the negative $pCO_{2,sw}$ bias in these regions. These biases induce air-sea pCO_2 gradients that are positive (atmospheric pCO_2 greater than ocean pCO_2) in the model, whereas in observations they are negative. Notice that in the Southern ocean, the observed CO_2 flux is near-zero, so that it would only take a small bias in $pCO_{2,sw}$ for the model's Southern Ocean to become a region of atmospheric CO_2 uptake.

Table 2 lists the NRMSE and bias for each of the fields examined in this study. For $pCO_{2,sw}$, we find that the root mean square difference is only ~10% of the observed annual mean value. The bias is similarly small, being ~10 μatm. On the other hand, we find a large difference between model and observed fluxes: the root mean square difference

between simulated and observed fluxes is ~3× larger than the mean observed CO_2 flux (Table 2). The bias in the CO_2 flux is much smaller, ~ -0.1 g C/m^2/yr, which amounts to ~2% of the annual mean observed flux. These differences suggests that even though regional discrepancies in the CO_2 flux are large, the model does a better job at capturing the global CO_2 flux.

The normalized root mean square differences are larger for the CO_2 flux than the remaining BGC fields, and are much larger for the MLD, NPP, nitrate, and silicate than for temperature, salinity, alkalinity, DIC, and wind speed. The biases are small for all fields, except for (1) wind speed, where the bias approaches 20% of the observed annual mean, and (2) for nitrate, silicate, and NPP, where the biases are at least 50% of their respective observed annual means.

Table 2. Annual mean values, normalized root mean square errors (NRMSE), and global bias between model surface fields and observations discussed in this study.

	E2-R mean	E2.1-G mean	observed mean	NRMSE E2-R	NRMSE E2.1-G	bias E2-R	bias E2.1-G
CO_2 flux (g C/m^2/yr)	-3.36	-5.55	-5.63	1.79	2.94	1.92	-0.13
pCO_2 (μatm)	373	374	363	0.06	0.08	8.83	10.72
MLD (m)	91.13	66.53	66.11	1.05	0.85	-5.64	-1.32
NPP (g C/m^2/yr)	47.52	57.61	148.98	0.89	0.84	-101.77	-91.91
T (°C)	19.99	20.09	19.37	0.07	0.08	0.61	0.61
S (psu)	34.61	34.69	34.89	0.02	0.02	-0.27	-0.21
DIC (μmol/kg)	2028.21	2086.00	2043.88	0.02	0.03	-14.44	43.65
Alk (μeq/kg)	2029.40	2369.32	2309.02	0.02	0.03	-10.91	59.22
Nitrate (μmol/kg)	3.42	1.33	4.95	0.60	1.19	-1.42	-3.37
Silicate (μmol/kg)	5.60	10.15	4.63	1.47	2.67	1.04	5.88
wind speed (m/s)	7.32	7.31	8.57	0.17	0.17	-1.23	-1.22

3.1.2 Changes from CMIP5

Table 2 also lists the global NRMSE and bias for fields from E2-R, the NASA-GISS CMIP5 submission (this model is described in further detail in Romanou et al. (2013)). The NRMSE and bias in $pCO_{2,sw}$ have increased by ~33% and ~22% from E2-R to E2.1-G, respectively. While the NRMSE for the CO_2 flux has increased by ~1.5, the bias has been reduced by >90%. Thus model skill in reproducing $pCO_{2,sw}$ has deteriorated overall, whereas for the CO_2 flux, the model has a reduced global bias at the expense of increased regional biases. These increased regional biases are most pronounced in the subpolar regions and Southern Ocean, where E2.1-G has stronger CO_2 sinks, in the equatorial Atlantic, where it has a stronger CO_2 source, and in the equatorial Pacific (Fig. 1b,c; 2a,b), where it has a weaker CO_2 source. Moreover, the NRMSE and bias in DIC, alkalinity, and macronutrient concen-

trations in E2.1-G show large increases, from 50% to 300% of these respective metrics in E2-R. On the other hand, NPP shows slight improvement in E2.1-G, with a decrease in the NRMSE of ~6% and bias by ~10%. The main improvements in NPP are in the Southern Ocean and equatorial Pacific, which show higher productivity compared to E2-R and similar productivity compared to (though slightly higher than) observations (Fig. 1e, 2d).

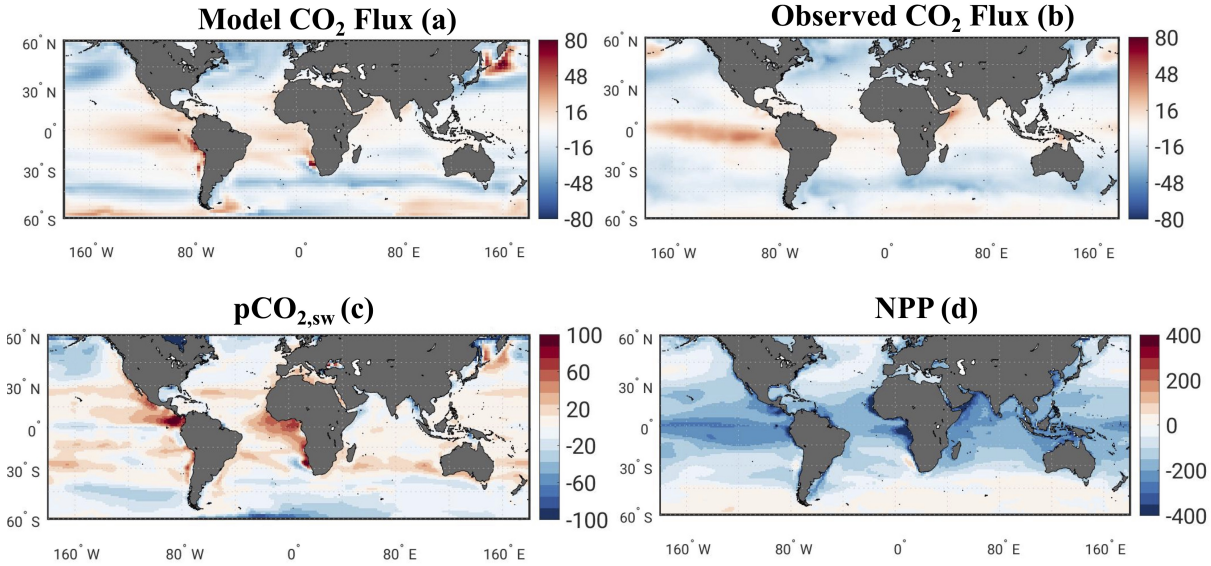

Figure 2. The first two panels show the air-sea flux CO_2 (g C/m^2/yr) (a) from model E2-R and (b) from the annual climatology of Landschützer et al. (2014). Positive values represent outgassing. The other panels show biases between the E2-R and the observed annual climatologies of (c) $pCO_{2,sw}$ (μatm) and (d) net primary production (g C/m^2/yr).

3.2 Seasonality during observational periods

In this section, we provide an overview of the time-averaged seasonal cycles of the CO_2 flux and ΔpCO_2 in each of the regions examined in this study. We also discuss the biases in both of these seasonal cycles and use an analysis based on first-order Taylor series expansions to attribute these biases to one or a combination of biases in the fields that impact the CO_2 flux and ΔpCO_2. To this end, we also show the seasonal cycles of the properties presented in Fig. 1, including the mixed-layer depth (MLD), sea surface temperature, sea surface salinity, net primary productivity (NPP), sea surface DIC, sea surface alkalinity, and surface wind speed. While not directly causing changes in ΔpCO_2, the roles of nitrate and silicate may also be important in seasonally and regionally limiting NPP, and thus drawing down sea surface DIC and $pCO_{2,sw}$. Hence we also present these macronutrients in the supporting information (Fig. S4-S6).

3.2.1 Seasonal Cycles

Subtropical Gyres: The simulated seasonal cycle of ΔpCO_2 and the CO_2 flux shows good agreement with the observations (Fig. 3a), with wintertime ΔpCO_2 and CO_2 flux minima and summertime ΔpCO_2 and CO_2 flux maxima. The ΔpCO_2 and CO_2 flux seasonal cycles are out-of-phase with the seasonal cycle of mixed layer depth, wind speed, and DIC (Fig. 3c,i), and in-phase with sea surface temperature (Fig. 3e,g). The seasonal cycles of alkalinity and salinity are small in both the model and the observations. Contrary to a large bias in the annual mean (discussed in the previous section), the net primary production (NPP) seasonality is realistic in the northern hemisphere basins of the Atlantic and the Pacific but it is out of phase from the observations in the respective southern hemisphere basins.

Equatorial regions: In the equatorial Atlantic and Pacific, the simulated seasonality of ΔpCO_2 (Fig. 4b) is more pronounced than in observations. In both of these regions, the model ΔpCO_2 minima occur ~4 months earlier than in observations. The month of maximum CO_2 uptake in the model also occurs ~4 months earlier than in observations in both regions. Unlike for ΔpCO_2 in the equatorial Pacific, the CO_2 flux in this region shows weaker seasonality in the model than in observations. The model boreal summertime minima in ΔpCO_2 and the CO_2 flux (Fig. 4a,b) across the equatorial regions are associated with increased trade wind speeds which lead to deepening of the mixed layer depth (Fig. 4c) and colder SSTs (Fig. 4e). Surface DIC and alkalinity in the model show much lower seasonal variability compared to observations in the equatorial Pacific (Fig. 4g). In the equatorial Atlantic, on the other hand, both the model and observations show maxima in DIC and alkalinity in austral winter and minima in boreal summer. However, in boreal summer and fall, there is higher monthly variability in observed vs. simulated alkalinity and DIC. NPP in the model fails to capture the observed seasonal variations in both equatorial regions (Fig. 4d). In the equatorial Pacific, the NPP maximum is ~6 months out of phase with observations, while in the equatorial Atlantic its seasonal amplitude is much lower than observed.

Subpolar regions and Southern Ocean: In both the subpolar North Atlantic and Pacific, the seasonal cycles of both ΔpCO_2 and the flux are quite different than in observations. Observations show ΔpCO_2 maxima in late boreal winter, while the model maxima are shifted by ~6 months compared to the observations. The model also produces ΔpCO_2 minima in boreal fall in both regions that are not observed. The corresponding observed CO_2 flux shows minima twice per year, in May and in October, and maxima in February and August. While the August CO_2 flux maximum is reproduced by the model in both regions, the model cannot reproduce the February maximum or May minimum in either re-

gion. The October minimum in the CO_2 flux is captured by the model in the subpolar North Pacific, but not the subpolar North Atlantic.

In the subpolar North Atlantic, the model shows a decrease in ΔpCO_2 from late boreal summer to boreal fall/winter, whereas in observations ΔpCO_2 continues to increase through boreal fall and winter. While the model and observations show similar changes in temperature during the period (Fig. 5e), the model shows a smaller change in DIC, by about ~30 μmol/kg, while observations show a ~50 μmol/kg change. The larger increase in observed DIC causes ΔpCO_2 to increase in observations, whereas in the model ΔpCO_2 slightly decreases due to an increase in solubility that overcompensates the increase in DIC. Interestingly, the model shows a smaller DIC change from boreal summer to winter despite having a much larger increase in the mixed-layer depth. The difference in boreal summer to winter DIC change is explored further in section 4.1. The model decrease in ΔpCO_2 in boreal winter, combined with the decrease in wind speed, results in stronger uptake in boreal winter vs. summer (Fig. 5a). In the subpolar North Pacific the large discrepancy between modeled and observed boreal wintertime ΔpCO_2 (Fig. 5b) coincides with the slightly larger than observed mixed layer depth (Fig. 5c) and the period when the model positive alkalinity bias is largest (Fig. 5g,h). DIC and alkalinity have opposite effects on ΔpCO_2; while increasing DIC increases ΔpCO_2, increasing alkalinity decreases ΔpCO_2. The overestimation of alkalinity that is brought to the surface leads to lower ΔpCO_2 and stronger uptake than in observations.

In the Southern Ocean, ΔpCO_2 and the CO_2 flux show similar seasonal patterns and biases. The air-sea flux of CO_2 indicates maximum uptake in late austral summer/early fall (Fig. 5a,b) and minimum in late austral winter. The timings of the peaks in the seasonal cycles of both CO_2 fields is shifted by about a month in the model compared to the observations, while the amplitudes of these seasonal cycles are also larger in the model compared to those in observations. There is also a shift in the timing of the peak in primary production, but unlike for the CO_2 fields, model peak NPP occurs earlier, rather than later, in the year compared to observations (Fig. 5d). The seasonal cycle of the remaining fields is reproduced well by the model, including the mixed layer depth, sea surface temperature, DIC, and wind speed (Fig. 5c,e,g,i). Both model and observations show almost no seasonal variations in alkalinity (Fig. 5h).

3.2.2 Changes in seasonality from CMIP5

In this section, we present the seasonality of the CO_2 flux and $pCO_{2,sw}$ in E2-R and compare these seasonal cycles to those from observations and E2.1-G. The seasonal amplitudes and timing of seasonal extrema of the CO_2 fields are presented in Fig. 6c-f, while

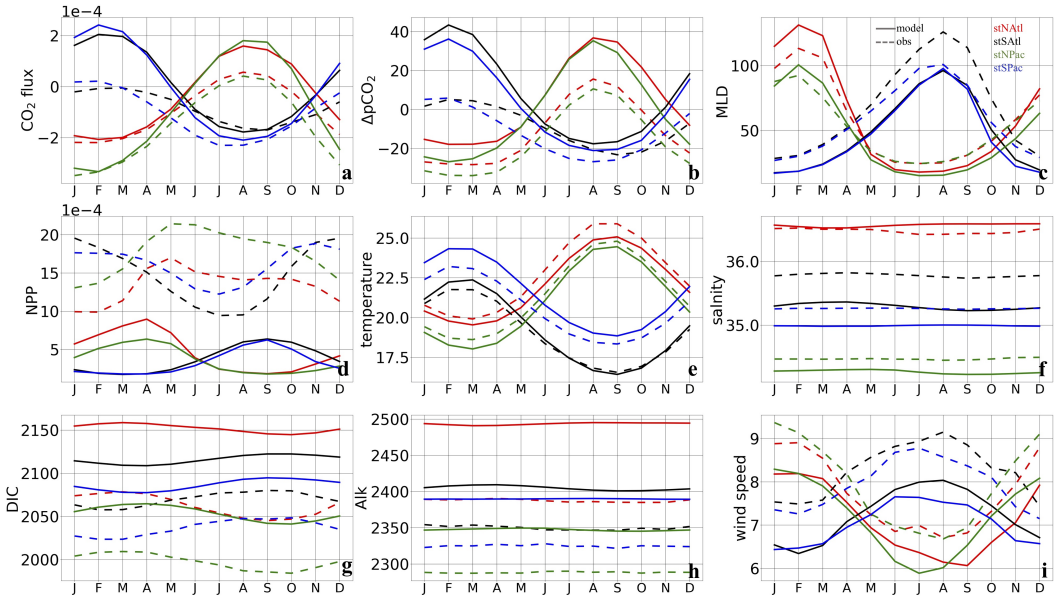

Figure 3. Seasonal cycles of (a) the air-sea CO_2 flux (Pg C/yr; positive values represent outgassing, negative values represent uptake), (b) difference between sea surface and atmospheric pCO_2 (μatm), (c) mixed-layer depth (m), (d) net primary production (Pg C/yr), (e) sea surface temperature (^{o}C), (f) sea surface salinity (psu), (g) sea surface dissolved inorganic carbon (μmol/kg), (h) sea surface alkalinity (μeq/kg), and (i) surface wind speed (m/s) in the subtropical regions. In each panel, the dashed lines correspond to the observations (see section 2.2), and solid lines are the simulated values from the historical run averaged over the period of the respective observations. In the legend "stNatl" is subtropical North Atlantic, "stNPac" is subtropical North Pacific, "stSPac" is subtropical South Atlantic, and "stSPac" is subtropical South Pacific.

the seasonality of other fields are shown in Fig. S8-9. For ease of comparison of annual mean to seasonal cycle properties, we also show the annual means for each region in Fig. 6a-b, and Fig. S7. For $pCO_{2,sw}$, the (N)RMSE and biases of the seasonal cycle (seasonal amplitude and timing of seasonal extrema) in E2.1-G are nearly the same as for E2-R (Table 3; for the timing of extrema, we use the RMSE instead of the NRMSE, since timing for all fields are in units of months). One exception is the bias in the timing of seasonal $pCO_{2,sw}$ extrema, which has been reduced by ~10% in E2.1-G from E2-R. The seasonal cycle of the CO_2 flux, on the other hand, has generally improved in E2.1-G compared to that of E2-R. The (N)RMSE and bias of the seasonal amplitude of the flux are smaller in E2.1-G than E2-R by ~33% and ~20%, respectively. The RMSE and bias for the timing of the seasonal CO_2 flux extrema have increased, but by only 1-2%. Overall, Table 3 indicates that on a global scale the model's skill in capturing the seasonal cycle of $pCO_{2,sw}$ remains largely unchanged between E2-R and E2.1-G, while its skill in capturing the seasonal cycle of the CO_2 flux has improved. The largest improvements (change in bias from E2-R to E2.1-G >10%) in the CO_2 flux seasonal amplitude are in the subpolar regions, subtropical North

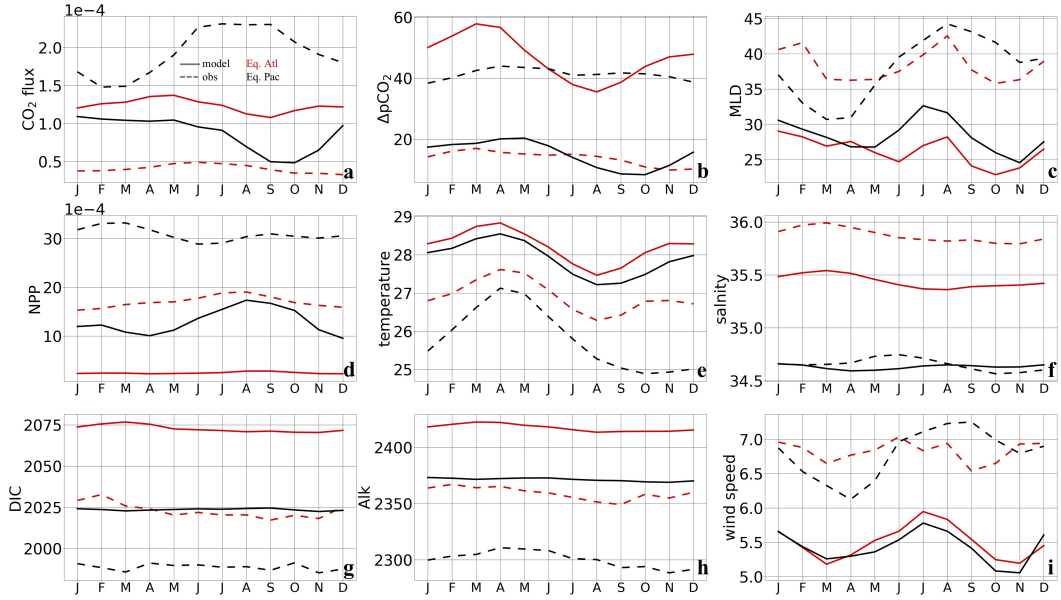

Figure 4. Same as Fig. 3, but for the equatorial regions. In the legend "EqAtl" is Equatorial Atlantic, and "EqPac" is equatorial Pacific.

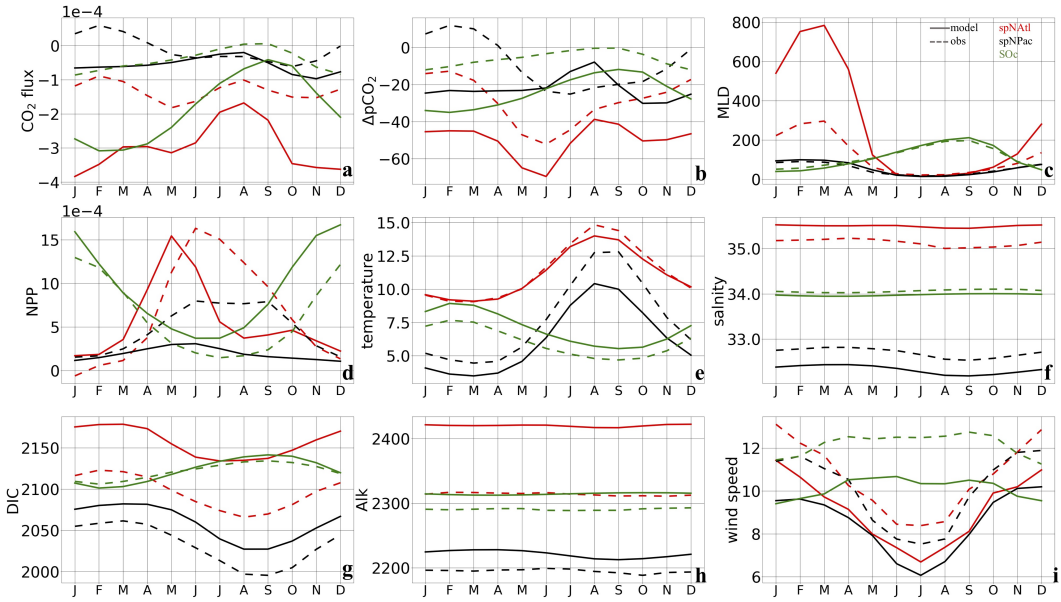

Figure 5. Same as Fig. 3, but for the subpolar regions and Southern Ocean. In the legend "spNAtl" is subpolar North Atlantic, "spNPac" is subpolar North Pacific, "SOc" is the Southern Ocean.

Pacific, subtropical South Pacific, and Southern Ocean, while model skill in capturing the seasonal amplitude of the flux has decreased in the equatorial regions and subtropical South Atlantic. The bias in the seasonal extrema timings have been reduced from E2-R to E2.1-G in the subtropical North Atlantic, subtropical North Pacific, subtropical South Atlantic, and Southern Ocean while it has increased in the subpolar regions and subtropical South

Pacific. The seasonal amplitude of $pCO_{2,sw}$ also shows an improved fit to observations in the subpolar regions, while biases in the seasonal amplitudes of this field have increased in the equatorial Atlantic and subtropical South Atlantic (Fig. 6b). The largest improvements in the seasonal extrema timings of $pCO_{2,sw}$ are in the subpolar North Atlantic and Southern Ocean, while the timings have deteriorated in the subpolar North Pacific.

Interestingly, while the NRMSEs and biases of annual mean DIC and alkalinity are larger in E2.1-G than E2-R, the NRMSEs of their seasonal amplitudes are slightly smaller (by < 10%;Table 3). The timings of their seasonal extrema also show a better fit to observations in E2.1-G. However, this improvement is small, amounting to at most a 12% reduction in the bias of the timing for DIC (less than this for the other seasonal extrema timing metrics for DIC and alkalinity). Moreover, the biases in the seasonal amplitudes of both DIC and alkalinity show dramatic increases; for DIC the bias is inflated by a factor of ~35 (from a very small bias to one that is ~20% of the mean seasonal amplitude of DIC; Fig. S8), while for alkalinity the bias increases by a factor of ~3. Nitrate and silicate show an overall worse fit in their seasonal cycles to observations in E2.1-G vs. E2-R. The biases and RMSEs of the seasonal extrema, as well as NRMSEs of the seasonal amplitudes, for nitrate and silicate are largely unchanged between E2-R and E2.1-G. However, the biases of the seasonal amplitudes have increased by ~21% for nitrate and ~12% for silicate. Thus for macronutrients, DIC, and alkalinity, the seasonal amplitude biases show changes (increases) that are > 10%, with the remaining metrics showing comparatively small changes. Overall, then, Table 3 indicates a general decline in model skill for capturing the seasonal cycles of these four fields. Finally, E2.1-G displays only about half of the bias in NPP as that of E2-R, suggesting a pronounced improvement in the seasonal cycle of this field. However, the improvements for the other seasonal cycle metrics for NPP are more marginal (<10%). Fig. S8 shows that this improvement in the seasonal amplitude bias masks important regional variability in changes to model skill; while the seasonal amplitude of NPP has been improved in some regions (subpolar North Atlantic, subtropical North Atlantic, equatorial Atlantic, and equatorial Pacific), it has deteriorated in others (subtropical South Atlantic and Southern Ocean).

3.2.3 Drivers of seasonal pCO_2

The seasonality of ΔpCO_2 varies widely between regions both in the observations and in the model. Over the course of the seasonal cycle, the magnitude (by over a factor of 4 in some regions) as well as the sign of ΔpCO_2 can change so that a region may switch from an atmospheric CO_2 sink to source. $pCO_{2,sw}$ is a function of temperature, salinity, DIC, and alkalinity. The seasonality of any of these drivers can potentially impact $pCO_{2,sw}$

Table 3. Normalized Root mean square errors and global biases between model and observed seasonal amplitudes (s.amp.) and timings of seasonal extrema.

	NRMSE E2-R s. amp	**NRMSE E2.1-G s. amp**	**bias E2-R s. amp**	**bias E2.1-G s. amp**	**RMSE E2-R timing**	**RMSE E2.1-G timing**	**bias E2-R timing**	**bias E2.1-G timing**
CO_2 flux ($g\,C/m^2/yr$)	1.53	1.04	17.89	14.77	2.19	2.24	1.51	1.52
pCO_2 (μatm)	1.07	1.03	20.44	20.72	2.32	2.19	1.65	1.48
NPP ($g\,C/m^2/yr$)	0.94	0.90	-47.02	-22.00	2.78	2.92	2.15	2.37
T ($^\circ C$)	0.26	0.25	0.11	0.11	1.14	1.18	0.62	0.65
S (psu)	0.83	0.83	0.04	-0.01	2.50	2.55	1.91	1.91
DIC ($\mu mol/kg$)	0.52	0.49	-0.23	-7.41	2.26	1.99	1.62	1.41
Alk ($\mu eq/kg$)	0.71	0.64	-1.21	-4.22	2.97	2.93	2.41	2.35
Nitrate ($\mu mol/kg$)	0.83	0.90	-1.60	-1.95	2.93	2.90	2.32	2.30
Silicate ($\mu mol/kg$)	1.09	1.09	-5.01	-4.41	3.12	3.14	2.54	2.57
wind speed (m/s)	0.30	0.27	-0.15	-0.15	2.07	2.17	1.45	1.48

seasonality. In this section, we determine the main drivers of the seasonality (or monthly anomaly from the annual mean) of $pCO_{2,sw}$, which itself is critically important in determining the air-sea CO_2 flux. To determine the main drivers of surface seawater $pCO_{2,sw}$ anomalies, we construct a linear, first order Taylor series expansion for the monthly anomalies in pCO_2 (Lovenduski et al., 2007; Doney et al., 2009; Mogollón & Calil, 2018; Landschützer et al., 2018; Gallego et al., 2018):

$$\begin{aligned} \delta pCO_{2,sw,i} \quad = \quad & \delta T_i\left(\frac{\partial pCO_{2,sw}}{\partial T}\right) + \delta S_i\left(\frac{\partial pCO_{2,sw}}{\partial S}\right) + \\ & \delta DIC_i\left(\frac{\partial pCO_{2,sw}}{\partial DIC}\right) + \delta Alk_i\left(\frac{\partial pCO_{2,sw}}{\partial Alk}\right) + H.O.T., \end{aligned} \tag{2}$$

where i is an index for months (i =JAN,FEB...DEC), and $H.O.T$ stands for higher-order terms neglected in this analysis. The δ terms represent deviations from the annual mean, i.e.,

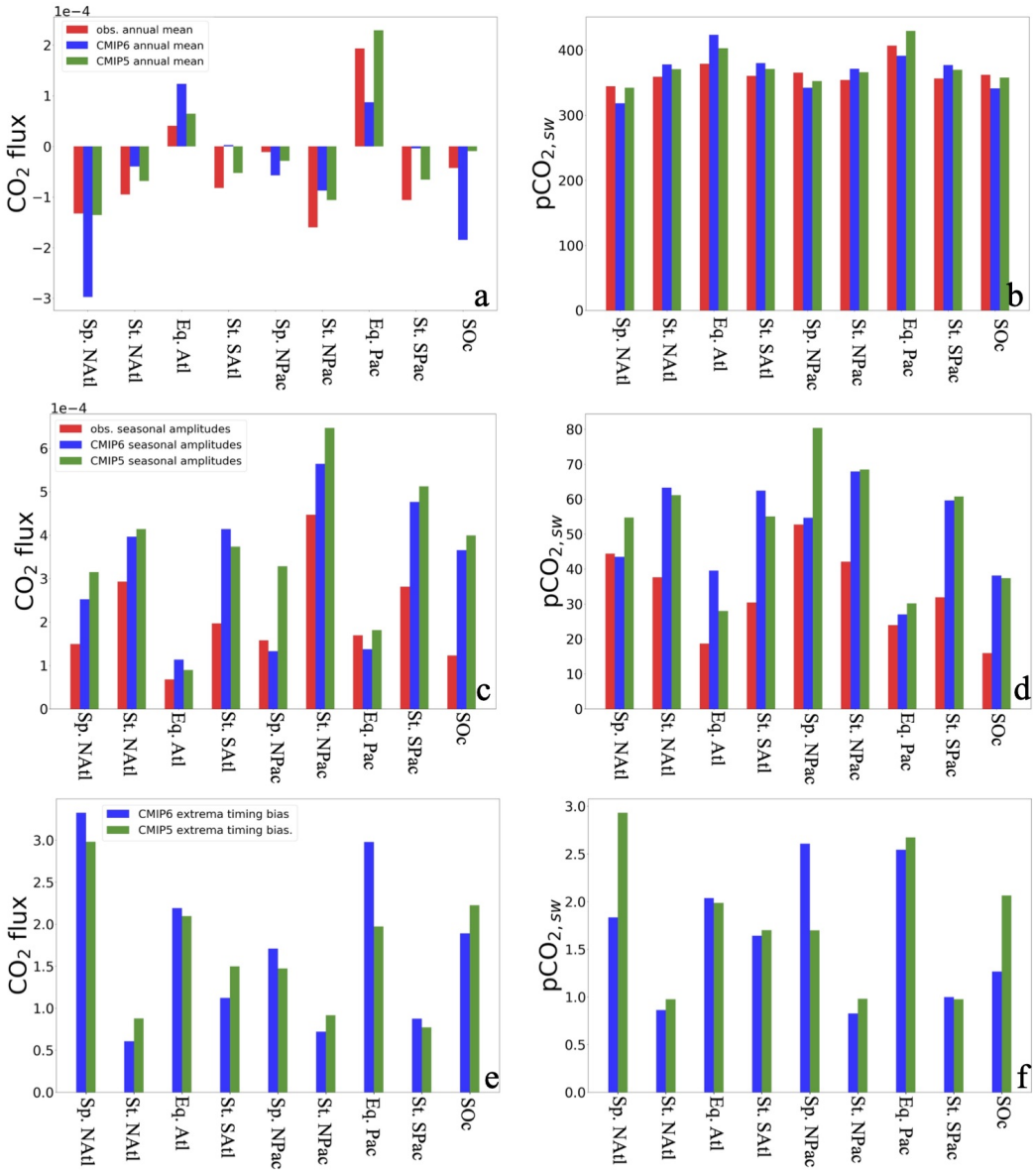

Figure 6. Seasonal cycle properties in observations, E2.1-G (CMIP6), and E2-R (CMIP5) in the CO_2 flux (Pg C/yr; panel a,c,e) and $pCO_{2,sw}$ (μatm; panel b,d,f). The top panels show the annual means in both the observations (red bars) and the models (E2.1-G as blue bars, E2-R as green bars). The middle panels show the seasonal amplitudes (seasonal maxima − minima) in observations as well as both models. The bottom two panels show the biases of the timing (in months) of seasonal extrema between E2.1-G and observations (blue) or E2-R and observations (green).

are obtained by differencing the (climatological) monthly (X_i) and annual mean fields ($\overline{X}$), so that $\delta X_i = X - \overline{X}$. The partial derivatives are obtained by (i) calculating $pCO_{2,sw}$ offline, (ii) adding a perturbation to each driver that amounts to 0.1% of their annual mean surface value, and recalculating the $pCO_{2,sw}$ offline (Mogollón & Calil, 2018), and (iii) taking the difference between perturbed and unperturbed $pCO_{2,sw}$. Both the model derived and

observed drivers are used to assess the right-hand side terms in (eq. 2). The dominant drivers of the seasonal cycle of $pCO_{2,sw}$ are those associated with the largest right-hand side terms. Similar methods based on Taylor series expansions have been used to assess drivers in the variability of $pCO_{2,sw}$ and the CO_2 flux (Lovenduski et al., 2007; Doney et al., 2009; Mogollón & Calil, 2018; Latto & Romanou, 2018). Offline calculations of $pCO_{2,sw}$ are performed using the OMIP-BGC carbonate chemistry protocols, which estimate $pCO_{2,sw}$ from CO_2^* (the sum of carbonic acid and dissolved CO_2) and the solubility of CO_2 by (i) calculating the solubility of CO_2 as a function of temperature and salinity (as for the CO_2 flux), and (ii) calculating CO_2^* from pH and DIC, where pH is obtained by solving the pH-alkalinity equation with the SolveSaphe algorithm (Munhoven, 2013; Orr et al., 2017).

In each region, we find that temperature and DIC play the dominant role in driving $pCO_{2,sw}$. While the temperature and DIC effects often oppose each other, they are seldom of the same strength such that alkalinity partially influences $pCO_{2,sw}$. The relative importance of these three drivers depends on the region and time of year, and varies between the model and observations.

In the subtropical regions (Fig. 7b,d,f,h), temperature drives the wintertime minimum and summertime maximum of $pCO_{2,sw}$ in both model and observations. However, the role of the DIC-driven anomalies, which act in opposite direction to the temperature-driven $pCO_{2,sw}$ anomalies, is underestimated in the model in the subtropical North Atlantic, South Atlantic, and South Pacific, leading to stronger seasonality in $pCO_{2,sw}$ in the model compared to observations in these regions (Fig. 3b). On the other hand, in the subtropical North Pacific, the contributions of DIC and temperature to the $pCO_{2,sw}$ anomalies agree with observations, although alkalinity contributes slightly more to the boreal summertime maximum and wintertime minimum in ΔpCO_2 in the model than in observations in this region.

In the subpolar regions (Fig. 7a,e) and the Southern Ocean (Fig. 7i), DIC plays a much larger role in driving the seasonal cycle of $pCO_{2,sw}$ in both the model and in observations, being commensurate to the role of temperature in the subpolar regions (Fig. 7a,e) and playing a larger role than temperature in the Southern Ocean (Fig. 7i). However, the model can often underestimate the DIC-driven $pCO_{2,sw}$ anomalies, resulting in differences between the model and observed seasonality of $pCO_{2,sw}$. For example, in late boreal summer in the subpolar North Atlantic, DIC drives negative $pCO_{2,sw}$ anomalies in observations, while in the model temperature drives positive $pCO_{2,sw}$ anomalies that overcompensate for the negative DIC driven $pCO_{2,sw}$ anomalies, so that the model shows a boreal summertime maximum in $pCO_{2,sw}$ and ΔpCO_2 (Fig. 5b). In boreal winter, both the

model and observations exhibit a DIC-driven $pCO_{2,sw}$ maximum, but this DIC-driven maximum is underestimated by the model.

Similarly, in the subpolar North Pacific in boreal summer the DIC driven minimum in $pCO_{2,sw}$ in the model is compensated by temperature and alkalinity effects on $pCO_{2,sw}$, which drive a maximum in model $pCO_{2,sw}$ (Fig. 5b). In observations, however, the alkalinity driven $pCO_{2,sw}$ anomaly is small in boreal summer, and the DIC driven anomaly is greater than the temperature driven anomaly, so that overall the observed $pCO_{2,sw}$ is higher on average during boreal summer. In the Southern Ocean, both the model and observations show DIC driven minima in $pCO_{2,sw}$ in austral summer and maxima $pCO_{2,sw}$ in austral winter, although the model DIC driven component in both seasons is greater in magnitude than observed. As elaborated in section 4.1, we speculate that the bias in the DIC-driven component of the $pCO_{2,sw}$ anomalies is due to overestimation of NPP in austral summer and overestimation of mixing of DIC from subsurface waters in austral winter.

Driver contributions in the equatorial regions are more complex. The dominant component of the seasonal cycle of $pCO_{2,sw}$ in these regions varies with time of year and differs between model and observations. In the equatorial Atlantic, temperature and DIC both drive a $pCO_{2,sw}$ maximum in early boreal spring (maximum delta pCO_2 in Fig. 4b), which is partially compensated by the effect of alkalinity driving $pCO_{2,sw}$ downward during the same season (Fig. 7c). In August, temperature drives a $pCO_{2,sw}$ minimum in the model in late boreal summer, whereas in observations the temperature effect is roughly compensated by the effect of alkalinity, so there is neither an observed $pCO_{2,sw}$ minimum nor maximum in August (Fig. 4b). Instead, there is an observed $pCO_{2,sw}$ minimum in November, driven by negative anomalies in observed temperature and DIC during this period. In the model, however, there is a positive temperature anomaly during this period which, combined with a positive alkalinity anomaly, drives a local $pCO_{2,sw}$ maximum in late boreal fall. In the equatorial Pacific, the temperature, DIC, and alkalinity driven $pCO_{2,sw}$ anomalies are generally smaller in magnitude in the model than in observations (Fig. 7g). In boreal spring, temperature drives a $pCO_{2,sw}$ maximum in both the model and observations. In early boreal fall, however, there is a mainly temperature driven minimum in $pCO_{2,sw}$ in the model, while in observations boreal fall minima in alkalinity and maxima in DIC drive positive $pCO_{2,sw}$ anomalies.

Importantly, in the equatorial Pacific, the drivers of the observed seasonal cycle of $pCO_{2,sw}$ must be viewed speculatively. The climatology of Takahashi et al. (2014) does not include DIC and alkalinity in the equatorial Pacific between 8°S and 8°N, due to the strong interannual variability in the measurements driven by El Ninõ and La Ninã events. Thus, the averages computed in Fig. 7g are biased to drivers of $pCO_{2,sw}$ outside of this equa-

torial band (in the model and in observations, since model averages were computed only using grid cells where observations are available). For example, the decrease in observed alkalinity in boreal fall, or "spike" in DIC in October, may not accurately reflect the seasonality of DIC and alkalinity of the entire equatorial Pacific, but only in the latitude bands outside of 8°S and 8°N. Given this observational uncertainty, it is unclear how well our model captures the seasonality of $pCO_{2,sw}$ in this region.

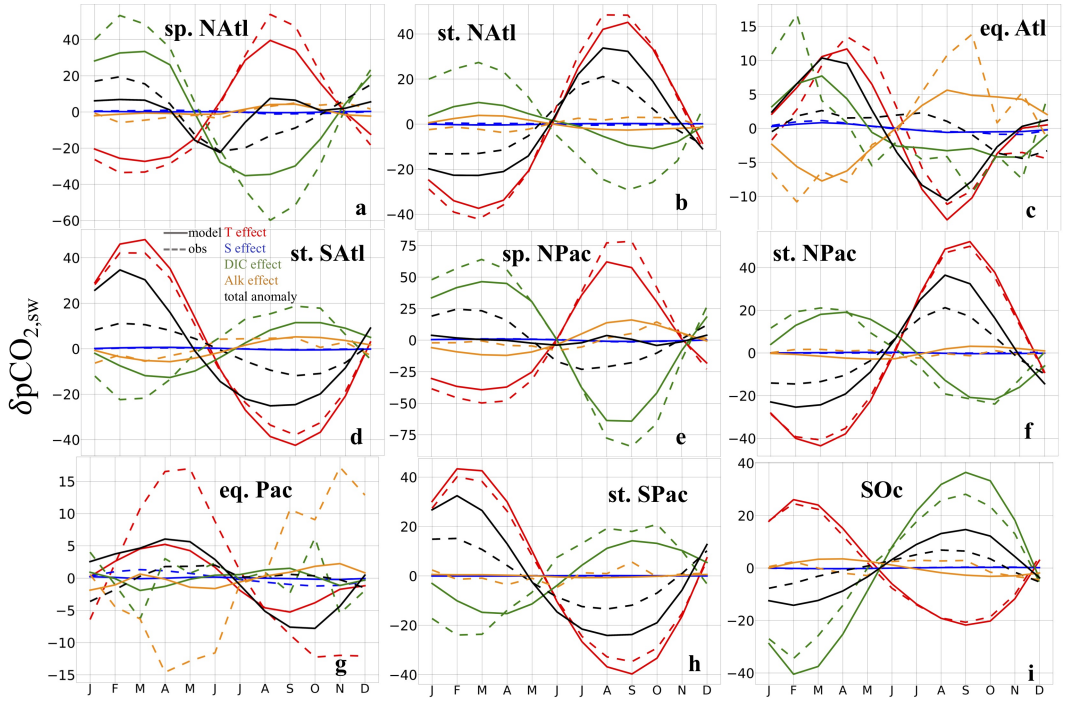

Figure 7. Monthly anomalies in $pCO_{2,sw}$ (μatm) driven by monthly anomalies in temperature (red lines), salinity (blue lines), DIC (green lines), and alkalinity (orange lines). Anomalies are shown for the subpolar North Atlantic and Pacific (a,e), the subtropical North Atlantic and Pacific (b,f), the equatorial Atlantic and Pacific (c,g), the subtropical South Atlantic and Pacific (d,h), and the Southern Ocean (i). In each panel, the dashed lines correspond to the observations (see section 2.2), and solid lines are the simulated values from the historical run. The black lines correspond to the modeled and observed total monthly anomalies of $pCO_{2,sw}$

3.2.4 Drivers of the seasonal CO_2 flux

As in the previous section, we evaluate the main drivers of the seasonality of the CO_2 flux using a Taylor series analysis. In this section, we only consider temperature and salinity effects imparted on the flux through the piston velocity and solubility, as their effects on ΔpCO_2 were detailed in the previous section. Similarly, we only consider the direct effect of wind speed on the piston velocity, as this analysis cannot account for wind-driven transport processes that also impact the air-sea exchange of CO_2. Both the piston veloc-

ity and solubility follow the protocols set for OMIP-BGC (Orr et al., 2017), and the calculation of the piston velocity uses the same quadratic gas transfer formulation as that used by Landschützer et al. (2014). The effect of sea ice is not considered, since in this analysis we exclude grid cells where seasonal sea ice is present.

To determine the dominant drivers of the CO_2 flux during the seasonal cycle, we employ a Taylor series expansion of the monthly anomalies in the flux:

$$\begin{aligned} \delta F_{CO2,i} &= \delta T_i(\frac{\partial F_{CO2}}{\partial T}) + \delta S_i(\frac{\partial F_{CO2}}{\partial S}) + \\ &\quad \delta Ws_i(\frac{\partial F_{CO2}}{\partial Ws}) + \delta \Delta pCO_{2,i}(\frac{\partial F_{CO2}}{\partial \Delta pCO_2}) + H.O.T. \end{aligned} \tag{3}$$

The procedure to estimate the right-hand side terms is largely the same as for $pCO_{2,sw}$. For the CO_2 flux anomalies, the partial derivatives are obtained by (i) calculating the CO_2 flux offline using the model's CO_2 flux routine, which follows the protocols for OMIP-BGC (Orr et al., 2017); (ii) adding a perturbation to each driver that amounts to 0.1% of their annual mean surface value, and recalculating the CO_2 flux offline, and (iii) taking the difference between perturbed and unperturbed CO_2 flux.

Figure 8 shows the monthly anomalies in the CO_2 flux (δF_{CO2} as computed from each term in eq. 3). The largest contribution to the flux anomaly reveals the dominant mechanism that determines the flux anomaly each month. In all regions, monthly anomalies in the CO_2 flux are driven mainly by wind speed and ΔpCO_2 (Fig. 8). Specifically, in the subtropical gyres (Fig. 8b,d,f,h) and in the Southern Ocean (Fig. 8i) the anomalies are nearly entirely driven by anomalies in ΔpCO_2. In the North and South Atlantic (Fig. 8b,d) and Pacific (Fig. 8f,h), in both model and observations, the summertime maximum and wintertime minimum in the CO_2 flux are driven by the maximum and minimum, respectively, in ΔpCO_2. However, in observations, the ΔpCO_2 driven anomaly in winter is smaller in magnitude than that in the model, which at least partly explains why the seasonality in the observed CO_2 flux is less than that in the model (Fig. 3a). Similarly, the austral summer minimum and winter maximum CO_2 flux in the Southern Ocean are driven by ΔpCO_2 in both the model and observations, although the wind speed appears to have a larger role in driving the seasonal variability of the flux in the model than in observations (Fig. 8i).

In the subpolar and equatorial regions, the CO_2 flux anomalies are driven by both ΔpCO_2 or wind speed depending on time of year, although the model and the observations do not always agree. In the subpolar North Atlantic in the model, the (late) boreal summertime maximum CO_2 flux (Fig. 5a) is driven mostly by wind speed (Fig. 8a). However, the contribution from the ΔpCO_2 driven flux anomalies in summer are not negligible. In boreal winter months, the simulated flux of CO_2 is more negative than in obser-

vations, due to the wind driven CO_2 flux anomalies being much larger in magnitude in the model than in observations. In the subpolar North Pacific, the model does not capture well the drivers of the monthly flux anomalies (Fig. 8e). Here, the simulated seasonal cycle of the CO_2 flux (maximum during boreal summer, minimum during boreal fall) is driven primarily by wind speed, and is opposite in phase to that of the observations, where the boreal summertime minimum and wintertime maximum flux are driven primarily by ΔpCO_2 (Fig. 8e).

In the equatorial Atlantic (Fig. 8d), the simulated flux has a realistic dependence to wind speed and ΔpCO_2. The boreal springtime maximum CO_2 flux (Fig. 4a,b) is driven by a boreal springtime maximum in ΔpCO_2, but this effect is more pronounced in the model than in the observations (Fig. 8c). However, in boreal summer, the model shows a CO_2 flux minimum driven by a ΔpCO_2 minimum, whereas observations show the flux to be higher than average (but not at a maximum) in boreal summer due a combination of above average ΔpCO_2 and above average wind speed.

Finally, in the equatorial Pacific, the model flux seasonal cycle is somewhat shifted compared to observations (Fig. 4a,b) and is dominated by ΔpCO_2 (Fig. 8g), while in observations, the flux seasonal cycle is controlled by the seasonal cycle of the wind speed. The discrepancy in the wind speed effect can be explained by considering that the CO_2 flux scales linearly with ΔpCO_2 and with the square of the wind speed (eq. 1). Thus the sensitivity (i.e., partial derivative) of the flux with respect to wind speed scales linearly with both ΔpCO_2 and the wind speed. Because in the equatorial Pacific both the wind speed and the magnitude of ΔpCO_2 are systematically underestimated by the model, the sensitivity of the CO_2 flux to wind speed is smaller in the model than in observations, leading to the model underestimating the effect of wind speed on the flux in this region.

3.3 Long Term Changes

3.3.1 Changes in Annual Means and Seasonal Amplitudes

In this section, we compare the change in model means and seasonal amplitudes of ΔpCO_2 and the CO_2 flux between the end of the historical period (1990-2014) and the run with 1% annual increase of atmospheric CO_2 after the pre-industrial era. For the latter run, we analyze results averaged over a 20 year period around the time of doubling of atmospheric CO_2 (i.e. simulation years 60-80). As in section 3.2.2, we define the seasonal amplitude as the maximum minus the minimum of a field's seasonal cycle in a certain period. The changes in model means and seasonal amplitudes of the CO_2 fields during each period are examined in each of the nine regions (Fig. 9). We provide the changes

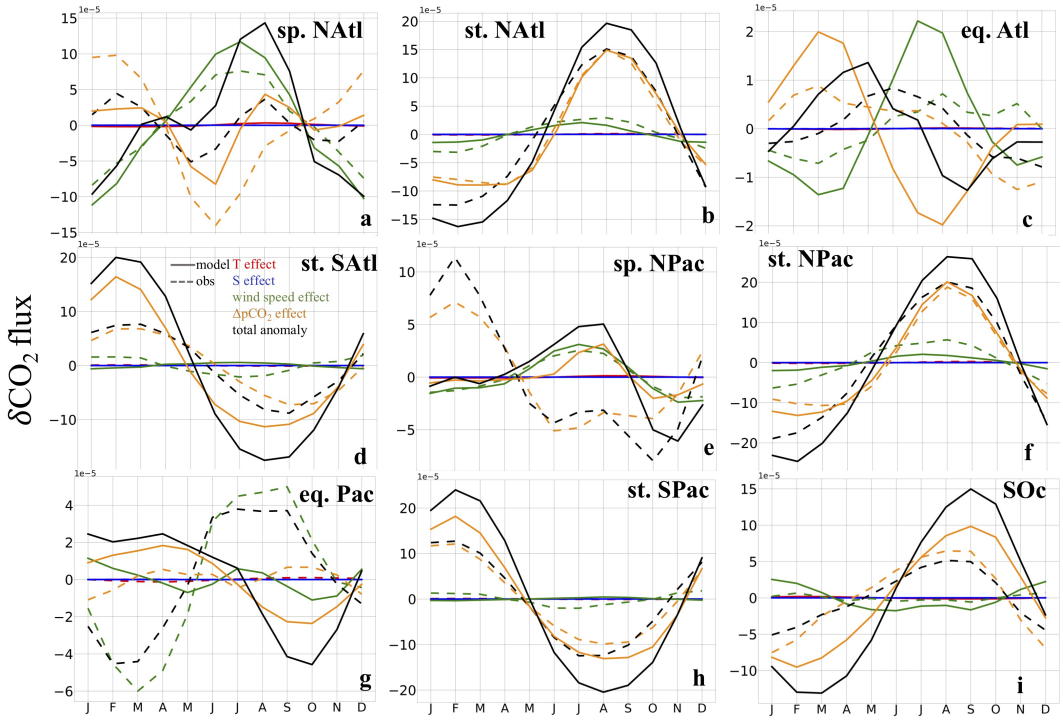

Figure 8. Monthly anomalies in the CO_2 flux (Pg C/yr) driven by anomalies in temperature (red lines), salinity (blue lines), wind speed (green lines), and ΔpCO_2 (orange lines). Anomalies are shown for the subpolar North Atlantic and Pacific (a,e), the subtropical North Atlantic and Pacific (b,f), the equatorial Atlantic and Pacific (c,g), the subtropical South Atlantic and Pacific (d,h), and the Southern Ocean (i). In each panel, the dashed lines correspond to the observations (see section 2.2), and solid lines are the simulated values from the historical run. The black lines correspond to the modeled and observed total monthly anomalies of the CO_2 flux.

in the model mean and seasonal amplitudes of all the surface properties in Fig. 3-5 in Fig. S10. The full seasonal cycle of the CO_2 fields, as well as the other aforementioned surface properties examined are provided in Fig. S11-S13.

All regions show a decrease in ΔpCO_2, with the largest change in the equatorial Pacific, and the smallest change in the subtropical North Pacific (Fig. 9b). The changes in the seasonal amplitude of ΔpCO_2 are larger than the mean changes everywhere except the tropical regions (Fig. 9b). The regions with the largest changes to the seasonal amplitude of ΔpCO_2 are the subpolar North Atlantic, subtropical North Atlantic, and Southern Ocean. In the subpolar and subtropical North Atlantic (Fig. S11a, S12a), the change in the seasonal amplitude is driven by an increase in the boreal summertime maximum and a decrease in the boreal winter minimum, while in the Southern Ocean it is driven by a decrease in the austral summer minimum (Fig. S13a). Consistent with the increase in ΔpCO_2, all regions show a tendency towards stronger uptake (Fig. 9a), with the largest changes occurring in the subtropical North Atlantic, subpolar North Atlantic, equatorial Pacific, and

Southern Ocean. Again, changes in the seasonal amplitude of the CO_2 flux are much larger than changes to the annual mean value in all except the equatorial regions (Fig. 9a).

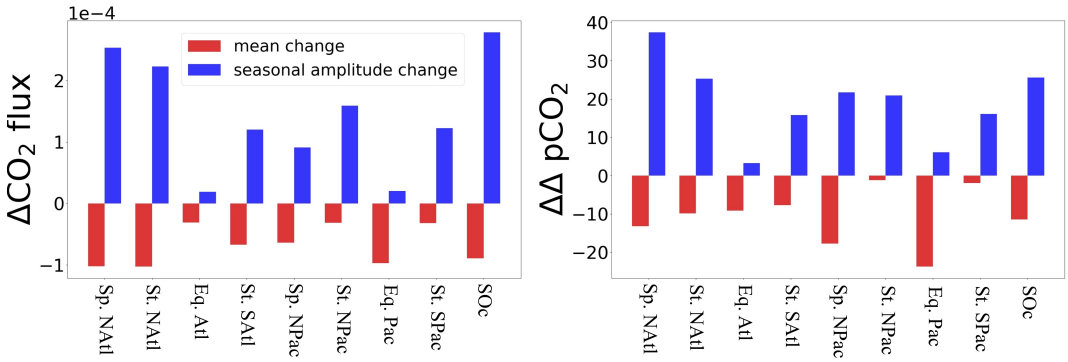

Figure 9. Changes in the mean (red) and seasonal cycle (blue) of CO_2 flux (Pg C/yr) (a) and ΔpCO_2 (μatm) (b) averaged between 1990-2014 in the historical simulation and averaged over 20 yrs centered around the time of doubling of the atmospheric CO_2 relative to its pre-industrial level in the 1% simulation (see section 2.3).

3.3.2 Drivers of Long Term Change in Seasonality

Since changes in the seasonal amplitude are found to be larger than changes in the mean state, we proceed to examine the drivers of the changes in the seasonality of $pCO_{2,sw}$ and the CO_2 flux. To this end, we expand the Taylor series of the change in $pCO_{2,sw}$ between the 1% and the historical (hist) simulations. The procedure for this Taylor series expansion follows previous studies on drivers of changes in the seasonality of the $pCO_{2,sw}$ (Landschützer et al., 2018; Gallego et al., 2018). For example, for a driver X for the $pCO_{2,sw}$ flux, we calculate the difference as:

$$\Delta\delta pCO_{2,sw,X,i} = \delta X_{2\times C,i}(\frac{\partial pCO_{2,sw}}{\partial X})_{2\times C} - \delta X_{hist,i}(\frac{\partial pCO_{2,sw}}{\partial X})_{hist}. \quad (4)$$

where δ represents the monthly change in the flux or its drivers and Δ represents the change between the two simulations. Equation 4 describes the difference in the monthly anomaly of the $pCO_{2,sw}$, as driven by property X, between the two experiments.

Continuing with our example using the $pCO_{2,sw}$ anomalies, the change in the anomalies driven by any given variable X can be further decomposed following a second Taylor series expansion:

$$\Delta\delta pCO_{2,sw,X,i} = \delta X_i(\Delta\frac{\partial pCO_{2,sw}}{\partial X}) + (\Delta\delta X_i)(\frac{\partial pCO_{2,sw}}{\partial X}) + H.O.T. \quad (5)$$

Here, the first term on the right-hand side represents the change in the monthly anomaly of $pCO_{2,sw}$ driven by X due to the change in the sensitivity of $pCO_{2,sw}$ to X, and the second term on the right hand side represents the change in $pCO_{2,sw}$ due to the change in the monthly anomaly in X. This analysis is applied to each driver of $pCO_{2,sw}$ (T, S, DIC, and Alk) and to each driver of the CO_2 flux (T, S, Ws and ΔpCO_2). This decomposition enables us to identify the drivers responsible for the changes in the seasonality of ΔpCO_2 and the CO_2 flux, as well as whether changes in the sensitivity to the drivers or the drivers themselves influence the change in the seasonality of the CO_2 fields.

We find regional variability in the main driver of the changes in the $pCO_{2,sw}$ anomalies (Fig. 10). In the subtropical regions (Fig. 10b,d,f,h), the main driver of the changes in the $pCO_{2,sw}$ anomalies is temperature, which tends to increase the $pCO_{2,sw}$ anomalies in the summer and decrease the anomalies occurring in winter. The largest contribution to the change in the temperature driven $pCO_{2,sw}$ anomalies is from the change in the sensitivity of $pCO_{2,sw}$ to temperature, as opposed to the change in temperature anomalies themselves.

In the subpolar North Pacific and the Southern Ocean, the main driver of the changes in the $pCO_{2,sw}$ anomalies is DIC (Fig. 10a,e,i), with the largest increase in the anomalies occurring in the winter for each basin and the largest decrease in the anomalies occurring in the summer. The largest contribution to the change in the DIC driven $pCO_{2,sw}$ anomalies in these two regions is from the change in the sensitivity of $pCO_{2,sw}$ to DIC, as opposed to the change in DIC itself. In the subpolar North Atlantic, the changes in the DIC driven $pCO_{2,sw}$ anomalies are also larger than the changes in $pCO_{2,sw}$ anomalies due to the other drivers (Fig. 10a). However, the combined change in the $pCO_{2,sw}$ anomalies due to alkalinity and temperature are larger than the DIC driven changes in the $pCO_{2,sw}$ anomalies, so that in this region the anomalies show the maximum increase in boreal summer and the anomalies show the maximum decrease in boreal winter. As in the subtropical regions, in the subpolar regions and Southern Ocean these changes are due to changes in the sensitivity of $pCO_{2,sw}$ to DIC, alkalinity, and temperature, with changes in temperature, DIC, and alkalinity themselves playing secondary roles (Fig. 10a,e,i).

In the equatorial regions, multiple drivers are important in influencing changes in $pCO_{2,sw}$. In the equatorial Atlantic in boreal winter, the increase in the DIC driven $pCO_{2,sw}$ anomalies is compensated by the decrease in the alkalinity driven $pCO_{2,sw}$ anomalies, whereas in boreal summer, the increase in the alkalinity driven $pCO_{2,sw}$ anomalies is compensated by the decrease in the DIC and temperature driven $pCO_{2,sw}$ anomalies (Fig 10c). In the equatorial Pacific, the temperature driven increase in the $pCO_{2,sw}$ anomalies in boreal spring and decrease in $pCO_{2,sw}$ anomalies in boreal summer are only partly offset by a concur-

rent decrease (increase) in the DIC driven $pCO_{2,sw}$ anomalies in boreal spring (boreal summer). This results in slightly larger changes in the seasonality of $pCO_{2,sw}$ in the equatorial Pacific than the equatorial Atlantic, though in both regions changes in the seasonality are small compared to the other regions (Fig. 10c,g). Like the other ocean regions, changes in seasonality in the equatorial regions are driven by changes in the sensitivity of $pCO_{2,sw}$ to its drivers, as opposed to changes in the drivers themselves themselves.

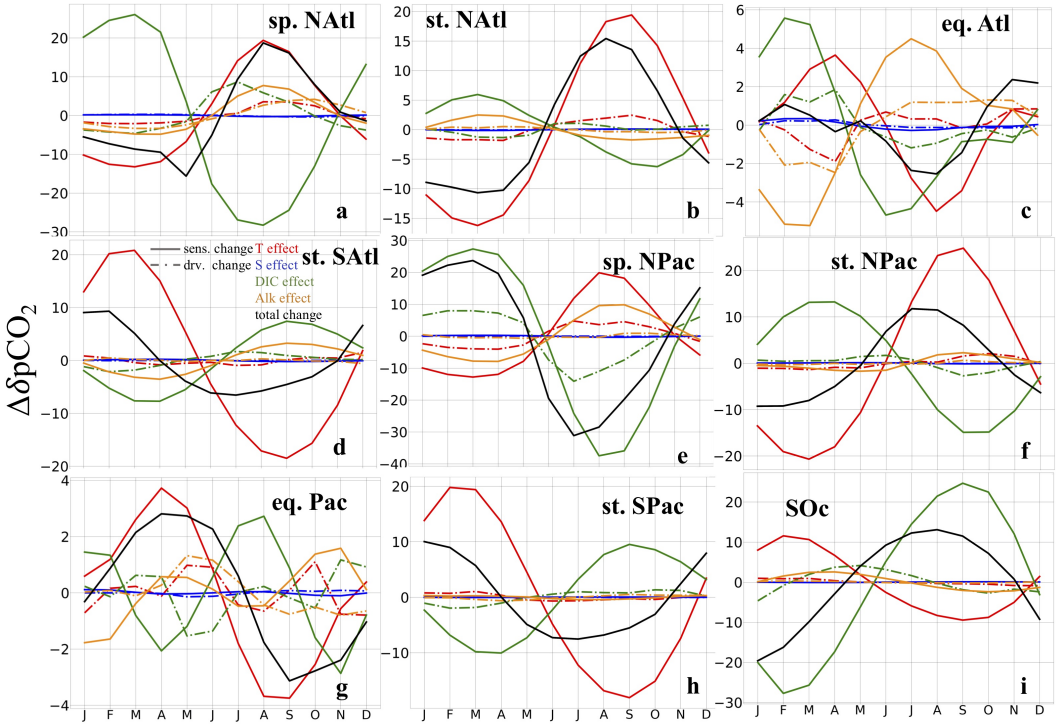

Figure 10. Contributions of changes in the sensitivities (partial derivatives, solid lines) and changes in the drivers (dashed-dotted lines) to changes in the monthly $pCO_{2,sw}$ (μatm) anomalies from the historical simulation to the 1% simulation driven by temperature (red), salinity (blue), DIC (green), and alkalinity (orange). Anomalies are shown for the subpolar North Atlantic and Pacific (a,e), the subtropical North Atlantic and Pacific (b,f), the equatorial Atlantic and Pacific (c,g), the subtropical South Atlantic and Pacific (d,h), and the Southern Ocean (i). The black lines correspond to the total change in the monthly anomalies of $pCO_{2,sw}$.

Turning to the CO_2 flux, in all regions except the equatorial regions, the changes in the CO_2 flux anomalies are driven by ΔpCO_2 (Fig. 11a,b,d,e,f,h,i). In each of these regions, the greatest contribution to the long term change in the ΔpCO_2 driven CO_2 flux anomalies is from the long term change in the monthly ΔpCO_2 anomalies themselves. The long term change in the sensitivity of the CO_2 flux to ΔpCO_2, on the other hand, plays a relatively minor role in affecting the long term change in the ΔpCO_2 driven CO_2 flux anomalies. In fact we see that the sensitivity of the flux to ΔpCO_2 changes little in the future. Changes

in ΔpCO_2 act to decrease the flux in the winter and increase it in the summer in the Atlantic regions and subtropical North and South Pacific. This is in contrast to the subpolar North Pacific and Southern Ocean regions, where changes in the ΔpCO_2 lead to increases in the flux during winter.

In the equatorial regions, the changes in the flux anomalies are driven by both ΔpCO_2 and wind speed (Fig. 11c,g). However, the drivers of the change to the wind-driven CO_2 flux differ between the two equatorial regions. In the equatorial Pacific during boreal summer and late fall, the change in the sensitivity of the CO_2 flux to wind speed, as opposed to the change in the wind speed anomalies themselves, mainly drives the change in the wind-driven CO_2 flux anomalies. However, during the rest of the year in the equatorial Pacific, and throughout the entire year in the equatorial Atlantic, the changes in the sensitivity to wind speed and wind speed anomalies play commensurate roles in driving the change to the wind-driven CO_2 flux anomalies. The opposite is the case for the ΔpCO_2 driven flux anomalies; the change in the flux anomalies are driven by the change in ΔpCO_2 anomalies. The maximum change in the flux anomalies occurs in boreal summer, with the flux anomalies decreasing due to an increase in the sensitivity to wind speed in June/July and to a decrease in the ΔpCO_2 anomalies in August/September. Note that the changes in the CO_2 flux anomalies are much smaller in the equatorial regions than the other regions, showing that there is little change in the seasonality of the CO_2 flux in the equatorial regions.

4 Discussion

We find that in the simulated seasonal cycle of $pCO_{2,sw}$, temperature tends to be the dominant driver in subtropical latitudes, the contributions of temperature and DIC are of similar magnitude in the northern subpolar regions, and DIC tends to be the dominant driver in the Southern Ocean (Fig. 7). Such a latitudinal contrast is not as apparent for the seasonal cycle of the CO_2 flux, which is controlled by ΔpCO_2 in the subtropical gyres, Southern Ocean, and subpolar North Pacific, but is driven nearly equally by wind speed and ΔpCO_2 in the subpolar North Atlantic (Fig. 8). In the equatorial regions, both the seasonal cycle of $pCO_{2,sw}$ and the CO_2 flux have drivers that are highly dependent on the time of year (Fig. 7,8). We also find that the long term change in the seasonal cycle of $pCO_{2,sw}$ is controlled by the same drivers that control its seasonal cycle at the end of the historical period (e.g., temperature in the subtropics and DIC in the Southern Ocean). Moreover, we find that the change in the sensitivity of $pCO_{2,sw}$ to the drivers, as opposed to changes in the seasonal cycles of the drivers themselves, control the long term change of the seasonal cycle of $pCO_{2,sw}$. For the CO_2 flux, we find that in all regions except the trop-

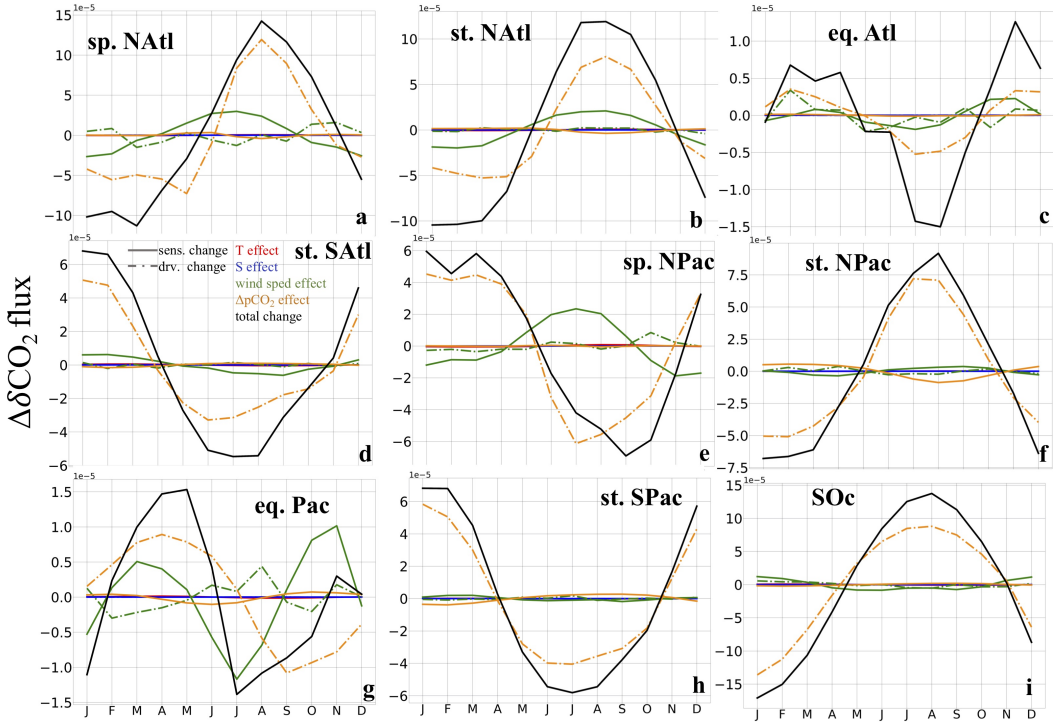

Figure 11. Contributions of changes in the sensitivities (partial derivatives, solid lines) and changes in the drivers (dashed-dotted lines) to changes in the monthly CO_2 flux anomalies (Pg C/yr) from the historical simulation to the 1% simulation driven by temperature (red), salinity (blue), wind speed (green) and ΔpCO_2 (orange). Anomalies are shown for the subpolar North Atlantic and Pacific (a,e), the subtropical North Atlantic and Pacific (b,f), the equatorial Atlantic and Pacific (c,g), the subtropical South Atlantic and Pacific (d,h), and the Southern Ocean (i). The black lines correspond to the total change in the monthly anomalies of the CO_2 flux.

ics, the long term change in the seasonal cycle of the CO_2 flux is controlled by changes in the seasonal ΔpCO_2 anomalies. However, these predicted long term changes must be viewed with caution, since the model's seasonal cycles and their drivers show major biases in multiple regions when confronted with observations. Below, we discuss the biases in the seasonal cycles in each of the drivers, focusing on the regions with the largest biases (equatorial Pacific and Atlantic, subpolar North and South Pacific, and Southern Ocean), and highlight processes that may produce these biases in the model. We then discuss changes in mechanisms driving the CO_2 flux from E2-R to E2.1-G, and speculate on changes in the model that may have led to different drivers between the two model versions. Finally, we analyze the mechanisms underlying the long term change of the sensitivity of pCO_2.

4.1 Discrepancies in the drivers of CO_2 seasonal cycles

In the model, the largest biases in the seasonal cycles of pCO_2 and the CO_2 flux occur in the non-subtropical gyre regions, including the equatorial Pacific and Atlantic, the

Southern Ocean, and the subpolar North Atlantic and Pacific. However, the biases are driven by different processes depending on the region considered. Table 4 summarizes the main drivers of the seasonal variability in $pCO_{2,sw}$ and the CO_2 flux in both the model and in observations. The dominant driver is reported in each region in boreal winter, boreal spring, boreal summer, and boreal fall.

Equatorial Regions: In the equatorial Pacific, much of the discrepancy between the model and observed CO_2 flux seasonality can be attributed to differences in the seasonality of ΔpCO_2 itself. Depending on the time of year, the model shows large biases in the temperature-driven, DIC-driven, and alkalinity-driven pCO_2 anomalies. For example, in late boreal fall, the model's temperature-driven pCO_2 anomalies are much smaller (closer to zero) than in observations (Fig 7g). The smaller than observed anomalies in temperature may be caused by the model underestimating upwelling in the eastern equatorial Pacific. This underestimation appears to be partially caused by the model having a more stratified eastern equatorial Pacific than in observations, with the model having warmer than observed waters above the thermocline and colder than observed waters below the thermocline (Fig. S14). In addition, notice that the maximum wind speed occurs in boreal summer in the model but it is sustained in boreal summer and fall in observations (Fig 4i). This suggests that wind-driven upwelling of cooler waters, which drives down $pCO_{2,sw}$, is restricted to a shorter period of time in the model vs. observations.

The observed DIC maximum in boreal late summer/early fall (Fig. 5g) is consistent with other modeling efforts examining the seasonal variability of $pCO_{2,sw}$ in the equatorial Pacific (Valsala et al., 2014; Wang et al., 2015), and has been attributed to the eastern equatorial upwelling during this part of the year. That the model cannot reproduce the DIC-driven $pCO_{2,sw}$ maximum in boreal fall (Fig 7g) may therefore also be a reflection of the model underestimating the contribution of upwelling to surface DIC. However, if upwelling were to drive the observed fall DIC maximum, one would also expect alkalinity to be maximum during this period, since upwelled waters should be enriched in both DIC and alkalinity. Instead, we find that in observations, alkalinity is below average in boreal fall (Fig. 4h). Since there is no observed NPP maximum in boreal fall, the observed lower-than average alkalinity may reflect the preferential growth of phytoplankton that are particularly efficient at removing alkalinity from the surface ocean, such as coccolithophores. The observation based seasonal cycles of alkalinity and DIC, however, are highly uncertain, given that their monthly climatologies do not include observations in the central equatorial pacific (Takahashi et al., 2014).

In our model, the seasonal variability of DIC and alkalinity is small compared to observations in the equatorial Pacific (Fig 4g,h). Similarly, the seasonal variability in the con-

tribution of alkalinity and DIC to the monthly $pCO_{2,sw}$ anomalies in the model is much smaller than observed (Fig 7g). To determine whether the lack of seasonal variability in model DIC and alkalinity is related to other sea surface properties (e.g. NPP), we re-calculate the average seasonal cycles of all properties shown in Fig. 4, but only at locations outside of the 8°S to 8°N band, where climatological values of DIC and alkalinity are present (Fig. S15). Aside from DIC and alkalinity, we find reduced seasonal variability in NPP and sea surface temperature compared to observations. Since primary production draws down both DIC and alkalinity, reduced seasonal variability in primary productivity may partly explain the reduced variability of DIC and alkalinity. The reduced variability in SST, on the other hand, may reflect a reduction in the variability of upwelling, which would reduce the contrast in SST during periods of maximum and minimum upwelling. Thus we speculate that reduced seasonal variability of both vertical transport and NPP contributes to the lack of seasonal variability in DIC and alkalinity in this region.

Aside from reduced seasonal amplitudes, the seasonality of the model's DIC and alkalinity is also out of phase with observations. In the model in boreal summer, upwelling appears to bring DIC and alkalinity to the surface (when the model reaches a temperature minimum; Fig S10e), resulting in DIC-driven and alkalinity-driven pCO_2 maxima and minima, respectively (Fig 7g). This is in contrast to observations, which show the period of maximum upwelling of DIC appears to be in boreal fall rather than summer (as suggested by the temperature minimum and DIC maximum; Fig. S15g,h). In boreal fall, the model shows maxima and minima in the alkalinity and DIC-driven $pCO_{2,sw}$ anomalies, respectively (Fig 7). These extrema are consistent with the model having (i) a lack of upwelling in boreal fall and (ii) having an NPP maximum in boreal fall (Fig 4d), which drives down both alkalinity and DIC. In contrast to the model, observations show lower than average NPP in boreal fall. This increase in model NPP, which is not observed, is likely due to (i) the model systematically underestimating nitrate throughout the year, and (ii) having a nitrate maximum associated with the model's late boreal summer upwelling (Fig S5). The systematic underestimation of nitrate makes some regions of the equatorial Pacific, such as the eastern upwelling region, nitrate limiting, when observations indicate that the eastern upwelling region of the equatorial Pacific should be iron limiting (Feely et al., 2002). Thus in the model, the pulse of nitrate that occurs in boreal summer (Fig S5) appears to promote the higher than average productivity in boreal summer and fall that is not observed.

There is a stark contrast in the role of wind speed in determining the seasonality of the CO_2 flux in the model and in observations. Throughout most of the seasonal cycle, wind speed dominates the seasonal cycle of the flux in observations but ΔpCO_2 is the main

driver in the model. The role of the model's systematically weaker winds and lower (in magnitude) ΔpCO_2 in lowering the magnitude of the wind driven CO_2 flux anomalies has already been mentioned in section 3.2.4. However, there are also discrepancies in the seasonal variation of the wind speed between the model and observations. For example, in early boreal fall the model has weaker than average winds, which drive a negative flux anomaly, whereas observations have stronger than average winds, which drive a positive flux anomaly (Fig. 8g).

Landschützer et al. (2013) reported that in the equatorial Atlantic, the thermal and non-thermal driven $pCO_{2,sw}$ changes roughly compensated one another, so that the net seasonal change is small. This is the case in our model as well, although there are clear biases in the alkalinity and DIC-driven components of $pCO_{2,sw}$. The largest biases in the components of the seasonal cycle of pCO_2 in the equatorial Atlantic occur in the alkalinity and DIC driven components during boreal summer. In observations, the alkalinity and DIC minima correspond to an NPP maximum in August, suggesting that productivity causes the extrema in the observed alkalinity and DIC-driven $pCO_{2,sw}$ in late boreal summer. In the model, however, no summertime NPP maximum is apparent, likely because the model has consistently low nitrate in this region throughout the year (Fig S5). Instead, model DIC and alkalinity-driven monthly $pCO_{2,sw}$ anomalies reach their minimum and maximum, respectively, earlier in boreal summer, although the cause of these extrema are not apparent from the sea surface properties examined in Fig 4.

There is broad similarity between the CO_2 flux and ΔpCO_2 observed and modeled seasonal cycles in the equatorial Atlantic, including the CO_2 flux and ΔpCO_2 trough in boreal fall and the CO_2 flux and ΔpCO_2 peak in boreal spring (Fig 4a,b). These extrema are similar to features found in previous modeling studies (Wang et al., 2015) and in other datasets (Lefèvre et al., 2013; Padin et al., 2010; Parard & Boutin, 2010). However, the drivers of the CO_2 flux are different between model and observations throughout the year (Table 4; Fig 8c). Both wind speed and ΔpCO_2 driven components of the flux are larger in magnitude in the model than in observations, though are generally of the same sign except in late boreal fall. This is consistent with the model having ΔpCO_2 that is systematically larger in magnitude than in observations, so that the sensitivity of the CO_2 flux to wind speed is larger in the model than in observations.

Subpolar North Atlantic and Pacific: In the subpolar North Atlantic and Pacific, both the model and observations show DIC-driven $pCO_{2,sw}$ anomaly maxima in boreal winter and temperature-driven anomaly maxima in boreal summer (Fig 7; Table 4). In the summer, DIC and temperature drive $pCO_{2,sw}$ anomaly extrema in the opposite direction to those in boreal winter. These extrema are due to convective mixing bringing cold deep waters

enriched in DIC to the surface (Miller et al., 1999), with the subsequent decrease in DIC in spring due to biological draw-down (Takahashi et al., 2002; Landschützer et al., 2014) and increased boreal summertime stratification. Key differences between the model and observations, however, are that the model shows smaller DIC-driven $pCO_{2,sw}$ extrema than observed in the subpolar North Atlantic, and larger alkalinity-driven $pCO_{2,sw}$ extrema than observed the subpolar North Pacific. In the subpolar North Atlantic, the model shows less seasonality in surface DIC because the vertical gradient in DIC in the top 1000 m is much smaller than in observations (Fig S1). The smaller vertical gradient means that although boreal wintertime mixing in the subpolar North Atlantic is larger than in observations, it does not increase DIC as much as in observations (Fig 5g). In the subpolar North Pacific, seasonality differences in $pCO_{2,sw}$ are more closely linked to seasonality differences in alkalinity. Like DIC, alkalinity is enriched in deep waters, so that in the model boreal wintertime mixing brings alkalinity to the surface (Fig 5h) and reduces $pCO_{2,sw}$. The model's negative alkalinity-driven $pCO_{2,sw}$ anomaly (Fig 7b) appears to be caused by the model having more alkalinity between 100-200 m than in observations (Fig S16). Thus, although the model and observed boreal wintertime mixed layer depth are similar (Fig 5c), the model overestimates the entrainment of alkalinity into surface waters during winter in the subpolar North Pacific.

The alkalinity-driven boreal summertime $pCO_{2,sw}$ maxima in the model in the subpolar North Pacific coincides with the period of maximum stratification, after the model's spring NPP maxima (Fig 5c,d). While increased NPP is responsible for the DIC minima in both the model and observations, only the model shows a productivity driven alkalinity minimum in boreal summer. This is likely because in the model, the processes affecting alkalinity and DIC are similar. Alkalinity calculations follow OCMIP2, which computes alkalinity based on the following assumptions: (i) alkalinity changes proportionally to the rate of change in phosphate (increasing phosphate decreases alkalinity), which itself is computed from the rate of change in nitrate scaled by the Redfield ratio, at each time step, (ii) calcium carbonate production (which decreases alkalinity) is proporitional to net primary production in the euphotic zone, and (iii) dissolution of calcium carbonate (which increases alkalinity) is proportional to the divergence of the downward flux of organic material (Najjar & Orr, 1999). Since biologically driven changes in alkalinity are largely proportional to biologically driven changes in DIC, it is somewhat expected that increasing NPP simultaneously decreases alkalinity and DIC in the model. However, in the real ocean, alkalinity changes are not only dependent on total productivity or the net divergence of organic material, but rather dependent on productivity of organisms chiefly responsible for alkalinity changes (e.g., particulate organic carbon forming organisms such as coccolithophores), and dissolution of calcium carbonate at depth. Thus, differences in the model

and observed alkalinity-driven $pCO_{2,sw}$ anomalies may partly be due to actual vs. modeled biologically driven alkalinity changes, in addition to differences in the transport of deep-ocean alkalinity to surface waters.

Finally, differences between model and observed alkalinity may also be related to salinity biases. For example, in the annual climatologies, alkalinity and salinity biases appear closely associated in the Gulf stream, near Central America, and in the southern tropical Pacific (Fig 1g,i). However, in the majority of the subtropical regions, alkalinity and salinity biases are opposite in sign. Moreover, in the subpolar North Pacific, there is little difference between the model and observed seasonal cycles of salinity, while observations show seasonality in alkalinity that is reduced compared to the model (e.g., no summertime minima; Fig 5f,h). Thus both the annual climatologies and seasonal cycles suggest that processes controlling salinity biases (e.g., differences in surface freshwater fluxes) only partially contribute to alkalinity biases.

In both the subpolar North Atlantic and Pacific, the model flux is shown to be more influenced by wind speed than the observed flux at all times except during boreal spring (Fig 8a,e; Table 4). Similar to the equatorial Pacific, the higher effect of wind speed occurs because the model overestimates the magnitude of ΔpCO_2 throughout most of the year (Fig 5b), leading to a higher sensitivity of the CO_2 flux with wind speed. The lower effect of ΔpCO_2 on the CO_2 flux in the model, on the other hand, is caused by the model underestimating wind speed throughout the year (Fig 5i), which lowers the model's sensitivity of the CO_2 flux to ΔpCO_2.

Southern Ocean: The model's seasonal cycle of $pCO_{2,sw}$ and the CO_2 flux is somewhat more consistent with observations in the Southern Ocean than in the other non-gyre regions. Minimum uptake and ΔpCO_2 both occur in late austral summer, with the CO_2 flux being ΔpCO_2 (Fig 8i) driven and $pCO_{2,sw}$ being DIC driven (Fig 7i). The non-thermal component of $pCO_{2,sw}$ drives the seasonal cycle through mixing of DIC to the surface in austral winter and DIC drawdown by biological utilization in austral summer (Landschützer et al., 2014; Pasquer et al., 2015; Mongwe et al., 2018; Gruber et al., 2019). Mongwe et al. (2018) has shown that the CMIP5 Earth System Models had difficulty capturing the seasonal cycle in the Southern Ocean, though in different ways. North of the Polar Front (where we restrict our analysis), some models overestimated the DIC-driven component of the seasonal cycle of $pCO_{2,sw}$ (3 of 10), while most models (9 of 10) overestimated the SST-driven component of the seasonal cycle. Our analysis shows that the SST driven anomalies in $pCO_{2,sw}$ are roughly consistent with observations, while the model generally overestimates the magnitude of the DIC-driven $pCO_{2,sw}$ anomalies in austral winter (Fig 7i). In austral winter, this overestimation may be due to the model overestimating the mix-

ing of DIC below ~100, since above 200 m (the average wintertime mixed layer depth in the Southern Ocean) in the Atlantic Sector of the Southern Ocean between 45^oN and 56^oN, the model overestimates DIC concentrations in subsurface waters (Fig S17). The apparent overestimation may also be an artifact of the lack of wintertime observations of DIC and pCO_2 in the Southern Ocean (Bakker et al., 2014; Lauvset et al., 2016). In austral summer, the model underestimation of the DIC-driven $pCO_{2,sw}$ anomalies may be due to the model having greater austral summertime NPP than in observations (Fig 5d).

In our analysis, we have separately examined the biases in the seasonal cycles in each region. However, a bias common to all regions in our model is the underestimation of nitrate. The underestimation of nitrate may partly explain the negative NPP bias in multiple regions, including the subtropical and equatorial reigons. Our model currently computes nitrogen fixation supported production based on iron and light availability, and does not include the effects of oxygen inhibition (Dunne & John, 2013). Furthermore, denitrification is not explicitly represented; instead, nitrate is removed in a given grid cell based on (i) the vertical integral of nitrogen fixation, and (ii) the ratio of nitrate in a grid cell to the vertical integral of nitrate. Nitrification is also not explicitly represented; instead, we assume that upon remineralization, ammonia is immediately converted to nitrate. Importantly, these representations of denitrification and nitrification do not account for their impacts on alkalinity. For example, denitrification should add alkalinity to the water column, while nitrification should remove alkalinity (Paulmier et al., 2009), but neither processes is accounted for in our model. Inclusion of a more realistic nitrogen cycle that includes oxygen inhibition for nitrogen fixation and an explicit representation of denitrification and nitrification may improve simulated nitrate values and allow for more realistic limitation regimes, improving DIC and alkalinity, and hence the air-sea exchange CO_2.

Table 4. Dominant drivers of anomalies in the CO_2 flux (outside parentheses) and $pCO_{2,sw}$ (inside paretheses) in each region. Drivers for pCO_2 are only given when pCO_2 is the dominant driver of the CO_2 flux. Dominant drivers are given for winter ("Win"), Spring ("Spr"), Summer ("Sum"), and Fall ("'Fal"). For the northern hemisphere and equatorial regions, winter is December-February, spring is March-May, summer is June-August, and fall is September-November. For the southern hemisphere, winter is June-August, spring is September-November, summer is December-February, and fall is March-May. Dominant drivers are denoted with a + if their associated anomalies averaged over a given season are positive, and a − if they are negative. Subscripts denote dominate drivers in E2.1-G, E2-R, and in observations (o).

Region	$Win_{E2.1-G}$	Win_{E2-R}	Win_o	$Spr_{E2.1-G}$	Spr_{E2-R}	Spr_o
subp NAtl	−Ws	−Ws	+pCO_2 (DIC)	+Ws	+Ws	−pCO_2 (DIC)
N Atl	−pCO_2 (T)	−pCO_2 (T)	−pCO_2 (T)	−pCO_2 (T)	−pCO_2 (T)	−pCO_2 (T)
Eq Atl	−Ws	−Ws	−Ws	+pCO_2 (T)	+pCO_2 (DIC)	+pCO_2 (T)
S Atl	+pCO_2 (T)	+pCO_2 (T)	+pCO_2 (T)	+pCO_2 (T)	+pCO_2 (T)	+pCO_2 (T)
subp NPac	−Ws	+pCO_2 (DIC)	+pCO_2 (DIC)	−Ws	+pCO_2 (DIC)	+pCO_2 (DIC)
N Pac	−pCO_2 (T)	−pCO_2 (T)	−pCO_2 (T)	−pCO_2 (T)	−pCO_2 (T)	−pCO_2 (T)
Eq Pac	+Ws	−Ws	−Ws	+pCO_2 (T)	+pCO_2 (T)	−Ws
S Pac	+pCO_2 (T)	+pCO_2 (T)	+pCO_2 (T)	+pCO_2 (T)	+pCO_2 (T)	+pCO_2 (T)
SOc	−pCO_2 (DIC)	−pCO_2 (DIC)	−pCO_2 (DIC)	− pCO_2 (DIC)	−pCO_2 (T)	−pCO_2 (DIC)

Table 4 continued

Region	$Sum_{E2.1-G}$	Sum_{E2-R}	Sum_o	$Fal_{E2.1-G}$	Fal_{E2-R}	Fal_o
subp NAtl	+Ws	+Ws	−pCO_2 (DIC)	−Ws	−pCO_2 (DIC)	+pCO_2 (DIC)
N Atl	+pCO_2 (T)	+pCO_2 (T)	+pCO_2 (T)	+pCO_2 (T)	+pCO_2 (T)	+pCO_2 (T)
Eq Atl	+Ws	+Ws	+Ws	−pCO_2 (T)	+pCO_2 (DIC)	−pCO_2 (DIC)
S Atl	−pCO_2 (T)	−pCO_2 (T)	−pCO_2 (T)	−pCO_2 (T)	−pCO_2 (T)	−pCO_2 (T)
subp NPac	+Ws	−pCO_2 (DIC)	−pCO_2 (DIC)	−pCO_2 (DIC)	−pCO_2 (DIC)	−pCO_2 (DIC)
N Pac	+pCO_2 (T)	+pCO_2 (T)	+pCO_2 (T)	+pCO_2 (T)	+pCO_2 (T)	+pCO_2 (T)
Eq Pac	−pCO_2 (T)	+Ws	+Ws	−pCO_2 (T)	−pCO_2 (T)	+Ws
S Pac	−pCO_2 (T)	−pCO_2 (T)	−pCO_2 (T)	−pCO_2 (T)	−pCO_2 (T)	−pCO_2 (T)
SOc	+pCO_2 (DIC)	+pCO_2 (DIC)	+pCO_2 (DIC)	+pCO_2 (DIC)	+pCO_2 (DIC)	+pCO_2 (DIC)

4.2 Changes in drivers of the CO_2 between CMIP5 and CMIP6

Table 4 also shows the dominant drivers of the CO_2 flux anomalies for E2-R. For most regions, the dominant drivers of the seasonal cycle of the CO_2 flux are the same between model versions. Exceptions are the subpolar North Atlantic in boreal fall, the equatorial Atlantic in boreal spring and fall, the subpolar North Pacific in boreal winter, spring, and summer, and the equatorial Pacific in boreal summer. For the subpolar North Atlantic, although both E2-R and observations show ΔpCO_2 to be the dominant driver of the monthly CO_2 flux anomalies in boreal fall, the ΔpCO_2-driven anomalies in E2-R are of opposite sign to those of observations. In contrast, the ΔpCO_2-driven anomalies in E2.1-G are of the same sign as those in observations, although are of smaller magnitude (Fig. 8a,S19a). The increase in the ΔpCO_2-driven anomalies in E2.1-G in boreal fall is due largely to an increase in the DIC-driven $pCO_{2,sw}$ anomalies during this season (Fig. 7a,S18a). While the seasonal amplitude of DIC in observations is better represented by E2-R than E2.1-G, the fall increase in DIC in E2-R lags the increase in observations by ~1 month. Thus, when DIC-driven $pCO_{2,sw}$ anomalies are averaged in boreal fall, they are negative in E2-R and positive in observations and (less so) in E2.1-G. In the equatorial Atlantic, ΔpCO_2 dominates the boreal fall and spring anomalies in the CO_2 flux in both models and observations. However, in boreal spring the $pCO_{2,sw}$ anomalies are driven by DIC in E2-R and temperature in E2.1-G and observations. This appears to be caused by the boreal spring temperature maximum being higher in E2.1-G and observations than in E2-R, thus driving a higher temperature-driven $pCO_{2,sw}$ maximum (Fig. 7c,S18c). In contrast, in boreal fall DIC drives the $pCO_{2,sw}$ anomalies in E2-R and observations, while for E2.1-G temperature continues to be the driver behind the $pCO_{2,sw}$ anomalies. While the temperature driven $pCO_{2,sw}$ anomalies are still better reproduced by E2.1-G than E2-R in boreal fall, the DIC-driven anomalies are better reproduced by E2-R, and in both E2-R and observations they are more negative than in E2.1-G. Notice also that alkalinity is also an important contributor to the seasonal cycle of $pCO_{2,sw}$ in the equatorial Atlantic in boreal fall, being of similar magnitude to DIC, and the alkalinity-driven $pCO_{2,sw}$ anomalies are better reproduced by E2-R than E2.1-G.

The subpolar North Pacific shows the largest number of changes in drivers of the CO_2 flux seasonal cycle between E2-R and E2.1-G, as these have changed in all seasons but boreal fall. Moreover, the dominant drivers in E2-R and observations are the same in all seasons, while they are only the same in boreal fall for E2.1-G. In the boreal winter and spring, wind speed is the dominant driver of the CO_2 flux in E2.1-G, and ΔpCO_2 is the dominant driver in E2-R and observations. This is due to a reduction in the seasonal amplitude of DIC in E2.1-G from E2-R (Fig. 7e,S8e,S18e), reducing its impact on the $pCO_{2,sw}$ anomalies in E2.1-G. Note also that the effect of temperature on $pCO_{2,sw}$ seasonality is

underestimated in E2.1-G (with a comparable bias to that of DIC), and comparable to observations in E2-R (Fig. 7e,S18e). Finally, in the equatorial Pacific, ΔpCO_2 is the dominant driver of the CO_2 flux anomalies in boreal summer in E2.1-G, while wind speed is the dominant driver in observations and E2-R. While the wind speed effect on the CO_2 flux anomalies is larger in observations that in E2-R during boreal summer, the discrepancy is increased in E2.1-G to the point that the anomaly is opposite in sign (Fig. 8g,S19g). The decrease in the wind-driven CO_2 flux anomalies are largely driven by the reduction in both the seasonal amplitude in wind speed and annual mean $pCO_{2,sw}$ (Fig. 6b,S8) in this region from E2-R to E2.1-G.

While in most regions and periods the drivers of the CO_2 flux have remained the same between E2-R and E2.1-G, in the regions and seasons in which they are different, E2-R generally shows a better match to observations. Changes in the model from E2.1-G to E2-R that altered the drivers remain a subject of future investigation. Some candidate model changes that may have contributed to differences between E2-R and E2.1-G drivers of the CO_2 flux seasonality include: (i) the implementation of exponential detrital sinking profiles, which may have changed the fraction of fixed carbon exported below the euphotic zone and hence surface DIC and nutrient concentrations, (ii) the inclusion of prognostic alkalinity, which appears particularly important in controlling $pCO_{2,sw}$ in the equatorial Atlantic, and (iii) changes in the parameterizations of vertical mixing and mesoscale eddies (Kelley et al., 2020). The latter may have impacted vertical and lateral transport of heat and DIC, contributing to the reduction temperature-driven and DIC-driven pCO_2 anomalies in the subpolar North Atlantic and Pacific.

4.3 Importance of $pCO_{2,sw}$ in Driving Seasonality Changes

A somewhat expected result is that, between the 1% and the historical simulation in E2.1-G, changes in the monthly anomalies in the ΔpCO_2 gradient drive changes in the CO_2 flux in nearly all regions (Fig 11). On the other hand, long term changes in $pCO_{2,sw}$ anomalies can be roughly divided by regions where the change is controlled by temperature and by DIC (Fig 10). Our findings are consistent with the currently observed changes in the seasonal cycle of $pCO_{2,sw}$, which show temperature dominated changes in the subtropical gyres and DIC+alkalinity driven changes in the subpolar regions and Southern Ocean (Landschützer et al., 2018).

We further find that it is the change in the sensitivity of $pCO_{2,sw}$ to temperature or DIC (i.e., the change in the partial derivatives of eq. 2), as opposed to the change in temperature or DIC anomalies, that drives the change in the $pCO_{2,sw}$ anomalies. This finding can be explained if we consider simple decompositions of the partial derivatives with

respect to temperature (Takahashi et al., 1993) and DIC (Gallego et al., 2018):

$$\frac{\partial pCO_{2,sw}}{\partial T} = \gamma_T pCO_{2,sw} \tag{6a}$$

$$\frac{\partial pCO_{2,sw}}{\partial DIC} = \frac{1}{\gamma_{DIC}} pCO_{2,sw} \tag{6b}$$

Here, γ_T and γ_{DIC} are factors that determine the sensitivity of $\frac{\partial pCO_{2,sw}}{\partial T}$ and $\frac{\partial pCO_{2,sw}}{\partial DIC}$, respectively, to $pCO_{2,sw}$. γ_T is a factor that has been shown experimentally to be independent of temperature (Takahashi et al., 1993). Hence, the increase in the sensitivity of $pCO_{2,sw}$ to temperature between the end of the historical and the 1% simulation at the time of doubling of atmospheric CO_2 is expected, given that increasing atmospheric CO_2 also increases $pCO_{2,sw}$ and inflates the right hand side of eq. 6a.

On the other hand, γ_{DIC} is a measure of the ocean's capacity to buffer changes in $pCO_{2,sw}$ due to the accumulation of atmospheric CO_2 (Egleston et al., 2010; Hauck & Völker, 2015). γ_{DIC} is related to the Revelle factor (R), the ratio of the relative change in $pCO_{2,sw}$ to the relative change in DIC ($R = \frac{\partial pCO_{2,sw}}{\partial DIC} \frac{DIC}{pCO_{2,sw}}$; Sarmiento and Gruber (2006)), as

$$\gamma_{DIC} = \frac{DIC}{R}, \tag{7}$$

where DIC is the annually averaged surface ocean DIC concentration. To determine the contributions of γ_{DIC} and $pCO_{2,sw}$ to the long term change of $\frac{\partial pCO_{2,sw}}{\partial DIC}$ requires an expression for R that can be evaluated at the end of the historical period and at the time of doubling of atmospheric CO_2. In seawater, the Revelle factor may be approximated as (Sarmiento & Gruber, 2006)

$$R = \frac{3(Alk)(DIC) - 2(DIC^2))}{(2DIC - Alk)(Alk - DIC)}, \tag{8}$$

where as for DIC, Alk is the annually averaged surface alkalinity concentration. Combining eq. 7 with eq. 8, we obtain the following expression for γ_{DIC}:

$$\gamma_{DIC} = \frac{(2DIC - Alk)(Alk - DIC)}{3Alk - 2DIC)}. \tag{9}$$

Using a Taylor series decomposition similar to those in section 3.3.2 (eq. 5) and eq. 9, we decompose $\frac{\partial pCO_{2,sw}}{\partial DIC}$:

$$\Delta\frac{\partial pCO_{2,sw}}{\partial DIC} = (\Delta\frac{1}{\gamma_{DIC}})pCO_{2,sw} + \frac{1}{\gamma_{DIC}}(\Delta pCO_{2,sw}) + H.O.T. \tag{10}$$

We find that the relative contributions of changes in γ_{DIC} and $pCO_{2,sw}$ to the change in $\frac{\partial pCO_{2,sw}}{\partial DIC}$ are regionally dependent (Fig 12). The differences between the two contributions are largest in the equatorial and subtropical regions, where the contribution of $pCO_{2,sw}$ is much larger than that of γ_{DIC}, and are very small in the high latitude regions, specifically the Southern Ocean and subpolar North Pacific. We also find that γ_{DIC} decreases in each region, which in turn contributes to an increase $\frac{\partial pCO_{2,sw}}{\partial DIC}$ following eq. 6b. In addition, the decrease in γ_{DIC} must be due to an increase in R, since the annually averaged DIC increases in each region (Fig S7g), and increasing DIC increases γ_{DIC}. Other studies have found that future changes in γ_{DIC} impact the sensitivity of $pCO_{2,sw}$ to DIC (Hauck & Völker, 2015; Fassbender et al., 2018). Using the MITgcm coupled to REcoM-2, Hauck and Völker (2015) found that between 2011 and 2100, the decrease in γ_{DIC} significantly contributed to the increase in the seasonal drawdown of $pCO_{2,sw}$ in the Southern Ocean, with the change in biological productivity playing a relatively minor role. Fassbender et al. (2018), while not explicitly estimating γ_{DIC}, used the ESM2M run under the RCP8.5 concentration pathway to investigate changes in the Revelle factor due to anthropogenic carbon invasion. They found that at sites in the Kuroshio extension, the subtropical North Atlantic, Irminger Sea, and south of the Antarctic Polar Front Ocean, R increased betwen 1860 and 2100, with the largest increases occurring at high latitudes (the Irminger Sea and Southern Ocean). They also emphasized that the effect of this increase in R is to magnify the sensitivity of pCO_2 to DIC. The result obtained in this study, that a decrease in γ_{DIC} (increase in R) results in an increase in $\frac{\partial pCO_{2,sw}}{\partial DIC}$, with the largest γ_{DIC}-driven magnifications being in the high-latitudes (specifically the Southern Ocean and subpolar North Pacific; Fig. 12), is consistent with these previous studies.

When examining changes in the seasonality of pCO_2 in seven globally-coupled CMIP5 models between averaging periods 2006-2026 and 2080-2100, Gallego et al. (2018) found that the effects of changes in $\frac{\partial pCO_{2,sw}}{\partial T}$ and $\frac{\partial pCO_{2,sw}}{\partial DIC}$ on the change in the seasonality of $pCO_{2,sw}$ were larger than the effect of changes in the seasonality of temperature and DIC, respectively. This is consistent with the results of our study (see section 3.3.2). Gallego et al. (2018) also found that the contribution to the changes in the $\frac{\partial pCO_{2,sw}}{\partial T}$ and $\frac{\partial pCO_{2,sw}}{\partial DIC}$ from changes in γ_T and γ_{DIC}, respectively, were small compared to the contribution from the changes in the annual mean $pCO_{2,sw}$ in most regions. Since Gallego et al. (2018) do not provide their estimates of the change in γ_{DIC}, we cannot compare them to the changes found in

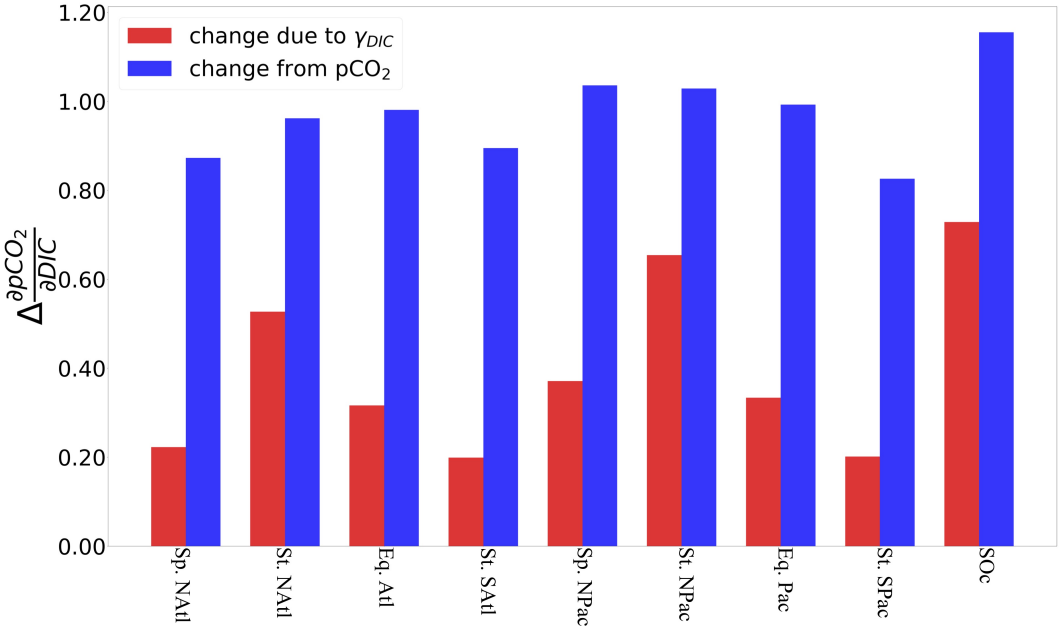

Figure 12. Contributions of the long term changes in $\frac{1}{\gamma_{DIC}}$ (red bars) and $pCO_{2,sw}$ (blue bars) to the long term changes in $\frac{\partial pCO_{2,sw}}{\partial DIC}$ (μatm/μmol) in each region. Changes are calculated as differences between quantities averaged over the historical and future climate periods described in section 2.3.

our study. Qualitatively, their results are consistent with those in our study, since the effect of the change in γ_{DIC} is smaller than that of the change in $pCO_{2,sw}$ in each region. Overall, the drivers of the change in seasonality in our model are consistent with those in the CMIP5 ensemble.

Landschützer et al. (2018) compared drivers of the change in the seasonality of the non-thermal component of pCO_2 averaged between 1985-1989 and between 2010-2014, based on integrating SOCATv4 $pCO_{2,sw}$ measurements into a neural-network. In their analysis, they decomposed the change in the monthly anomalies in non-thermal $pCO_{2,sw}$ into changes driven by the change in the Revelle Factor ($R = \gamma_{DIC} DIC$) and driven by changes in $pCO_{2,sw}$. They found that the Revelle-factor driven changes were about 1/2 of the $pCO_{2,sw}$ driven changes, and that the change in the annual mean $pCO_{2,sw}$ explained the majority of the change in the seasonality of $pCO_{2,sw}$ in the ocean, with the exception of the temperate latitudes in the southern hemisphere. They also found that at high latitudes, particularly near 60°N/S, the Revelle-factor driven changes are comparible with the $pCO_{2,sw}$ driven changes (see their Fig. S8). Thus drivers of changes in the seasonality of $pCO_{2,sw}$ obtained from the neural-network are generally consistent to those found here.

Two notes of cautions regarding our findings of long-term changes in the drivers of the seasonal cycles of $pCO_{2,sw}$ and the CO_2 flux should be considered. First, in regions

where the biases for both CO_2 seasonal cycles are largest, such as the subpolar North Atlantic and equatorial Pacific, the response of the drivers to changes in atmopsheric forcing in our model may under or overestimate the magnitude of the response in the real ocean. Second, it is unclear how robust the long term changes in drivers found in our model are. A rigorous measure of robustness (e.g., the internal variability of changes in the drivers) would require an ensemble of 1% simulations which are not available. Thus, while finding some consistency between our results and previous studies is encouraging, further investigation is required to constrain the uncertainty (both structural and due to internal variability) of the response of the seasonal cycle of the CO_2 flux and $pCO_{2,sw}$, as well as their drivers, to increases in atmospheric pCO_2. However, given the magnitude of the increase in atmospheric pCO_2 in the 1% simulation, we believe that this internal variability is overpowered by our forcing signal.

5 Conclusion

In this study, we have examined the seasonal cycles of $\Delta pCO_{2,sw}$ and the CO_2 flux in 9 different oceanic regions in the NASA-GISS modelE GCM (GISS-E2.1-G). We compared them to the seasonal cycles of an observation-based climatology as well as those in the NASA-GISS submission to CMIP5 (model E2-R), and identified the drivers of both the observed and modeled seasonal cycles using an analysis based on first-order Taylor Series expansions. We then examined the change in the seasonal cycle between two simulations: a historical simulation averaged between 1995-2014, and a simulation in which CO_2 reaches twice its pre-industrial value after increasing by 1% per year since 1850. Finally, we identified the drivers of the change in the seasonal cycles, elucidating the mechanisms by which the drivers change the seasonal cycles of the CO_2 flux and $pCO_{2,sw}$ between the historical and 1% simulations.

We found general improvement in the seasonal cycle of the CO_2 flux in E2.1-G compared to E2-R. However, when viewed at a regional level, changes in model skill in capturing the CO_2 flux seasonal cycle were much more heterogeneous. Five (three) out of the nine regions analyzed here showed a smaller (larger) bias in the seasonal amplitude, while four (three) of these regions showed a smaller (larger) bias in the timing of seasonal extrema. The seasonal cycle of $pCO_{2,sw}$ shows only marginal changes when viewing global skill metrics (Table 3). Regionally, the same number (three) of regions showed improvement and deterioration in the seasonal amplitude of $pCO_{2,sw}$, while the timing of seasonal extrema for $pCO_{2,sw}$ have improved (deteriorated) in 2 (1) regions. In addition, while the seasonal cycle of NPP shows a general improvement, the seasonal cycles of DIC, alkalinity, and macronutrients show a general reduction in model skill in E2.1-G compared to E2-

R. For E2.1-G, we found that the model seasonal cycles of the CO_2 flux and $pCO_{2,sw}$ showed similar phasing to the observed seasonal cycles, though with generally increased seasonal amplitudes, in the subtropical regions and Southern Ocean. In the subpolar and equatorial regions, the model was often out of phase with observations (e.g., CO_2 flux in the equatorial Pacific and ΔpCO_2 in the subpolar North Pacific), or did not exhibit the same number of extrema as observations (e.g., CO_2 flux in the subpolar North Atlantic). In most regions, we find that temperature and DIC play the dominant roles in driving $pCO_{2,sw}$ in both model and observations. However, the effects of DIC and temperature often oppose each other, such that in a few regions (e.g., Southern Ocean), alkalinity determines the seasonal cycle of $pCO_{2,sw}$.

In these regions of greatest disagreement, a combination of differences in model and observed DIC, temperature, and alkalinity-driven pCO_2 anomalies was responsible for the differences between the model and observed seasonal cycle of $pCO_{2,sw}$. In the subpolar regions, the largest differences were in the DIC and alkalinity components of the seasonal cycle of $pCO_{2,sw}$, while in the equatorial regions, the differences in the temperature, DIC, and alkalinity components of the seasonal cycle of $pCO_{2,sw}$ were of similar magnitude, but varied depending on the time of year. These differences reflect a combination of model biases in net primary productivity, transport of DIC, alkalinity, and nutrients to the surface ocean, and are also perhaps influenced by the lack of adequate observational data coverage in winter compared to summer. For the equatorial Pacific, they may also be influenced by the lack of climatological data for DIC and alkalinity. Future improvements to the model, including a particulate inorganic carbon tracer that would remove the dependence of alkalinity on total productivity, as well as explicit representations of denitrification and nitrification, should decrease these biases in the seasonal cycles.

When considering changes between the historical simulation and the 1% simulation, we found that in all regions, the ocean becomes a stronger atmospheric CO_2 sink, and the seasonality of ΔpCO_2 and the CO_2 flux increases in all regions except the subpolar North Pacific. However, the drivers of this stronger sink were regionally-dependent. The effects of temperature are most important in the subtropical regions, while the effects of DIC are most important in the subpolar North Atlantic and Southern Ocean. DIC, alkalinity, and temperature all have effects that are similar in magnitude on changes in ΔpCO_2 seasonality in the equatorial regions. However, a common thread in all regions is that changes in the seasonality of ΔpCO_2 are driven by changes in the sensitivity of $pCO_{2,sw}$ to changes in DIC, alkalinity, and temperature, as opposed to changes in the variables themselves. This finding is consistent with previous studies that show that the sensitivity of $pCO_{2,sw}$ to its drivers increase (i) as the seawater $pCO_{2,sw}$ concentration increases, and (ii) as the buffer

capacity of seawater decreases. These findings do not account for natural variability in the CO_2 flux, $pCO_{2,sw}$, or their drivers, since we only analyze a single historical and a single 1% simulation, and not an ensemble. Finally, we clarify that the aim of this paper is to document the advances and biases for only a single member of the CMIP6 ensemble. The documentation presented here should be useful for assessments of future GISS model development and for investigations across the climate modeling community seeking to interrogate the multi-model spread of the CO_2 flux and its seasonality in the CMIP6 ensemble. It should also be helpful for investigators attempting to understand processes that need to be better parameterized, and hence better constrained by observations, in order to reduce model bias and increase model skill in future projections of the CO_2 flux. To these ends, future studies should examine the response of the seasonality of surface ocean $pCO_{2,sw}$ and the CO_2 flux to climate change across the suite of CMIP6 models.

Acknowledgments

Funding was provided by the NASA-Modeling, Analysis Modeling and Prediction program (MAP) (grant number NNX16AC93G, under Principal Investigator Anastasia Romanou, and NNH10ZDA001N, under Principal Investigator Gavin Schmidt). Computational resources were provided by NASA Center for Climate Simulation High-End Computing Program through the NASA Center for Climate Simulation (NCCS) at Goddard Space Flight Center. We thank Ken Lo for submitting the NASA-GISS contribution to CMIP6, which includes the fields discussed in this study. We thank John Marshall for useful discussions on the model performance. We also thank the reviewers and associate editor for their constructive comments, which were greatly helpful in further improving the manuscript. All datasets used in this study are available from the NASA GISS climate group and through the CMIP6 repository (https://esgf-node.llnl.gov/projects/cmip6/). All methods, scripts and codes will be readily available though the GISS climate group repository. Access will be unrestricted at https://data.giss.nasa.gov/.

References

Bakker, D., Pfeil, B., K, S., Hankin, S., Olsen, A., Alin, S. R., ... Watson, A. J. (2014). An update to the surface ocean co2 atlas (socat version 2). *Earth System. Science Data*, *6*, 69-90.

Bopp, L., Resplandy, L., Orr, J. C., Doney, S. C., Dunne, J. P., Gehlen, M., ... Vichi, M. (2013). Multiple stressors of ocean ecosystems in the 21st century: projections with CMIP5 models. *Biogeosciences*, *10*, 6225-6245.

Bosilovich, M. G., Lucchesi, R., & Suarez, M. (2015). *MERRA-2: File Specification* [GMAO Office Note No. (Version 1.0)]. `http://gmao.gsfc.nasa.gov/pubs/office_notes`.

Boutin, J., Etcheto, J., Dandonneau, Y., Bakker, D. C. E., Feely, R. A., Inoue, H. Y., ... Wanninkhof, R. (1999). Satellite sea surface temperature: a powerful tool for interpreting in situ pCO_2 measurements in the equatorial Pacific Ocean. *Tellus B*, *51*(2), 490-508.

Copin-Montégut, C., & Raimbault, P. (1994). The Peruvian upwelling near 15 S in August 1986. Results of continuous measurements of physical and chemical properties between 0 and 200 m depth. *Deep Sea Research Part I: Oceanographic Research Papers*, *41*(3), 439-467.

Da Cunha, L. C., Buitenhuis, E. T., Le Quéré, C., Giraud, X., & Ludwig, W. (2007). Potential impact of changes in river nutrient supply on global ocean biogeochemistry. *Global Biogeochemical Cycles*, *21*(4), 1-15.

Doney, S. C., Lima, I., Feely, R. A., Glover, D. M., Lindsay, K., Mahowald, N., ... Wanninkhof, R. (2009). Mechanisms governing interannual variability in upper-ocean inorganic carbon system and air–sea CO_2 fluxes: Physical climate and atmospheric dust. *Deep Sea Research Part II: Topical Studies in Oceanography*, *56*(8-10), 640-655.

Doney, S. C., Ruckelshaus, M., Duffy, J. E., Barry, J. P., Chan, F., English, C. A., ... Talley, L. D. (2012). Climate change impacts on marine ecosystems. *Annual Review of Marine Science*, *4*, 11-37.

Dunne, J. P., & John, J. G. (2013). GFDL's ESM2 global coupled climate–carbon earth system models. Part II: carbon system formulation and baseline simulation characteristics. *Journal of Climate*, *26*(7), 2247-2267.

Egleston, E. S., Sabine, C. L., & Morel, F. M. (2010). Revelle revisited: Buffer factors that quantify the response of ocean chemistry to changes in DIC and alkalinity. *Global Biogeochemical Cycles*, *24*(1), 1-9.

Fassbender, A. J., Rodgers, K. B., Palevsky, H. I., & Sabine, C. L. (2018). Seasonal asymmetry in the evolution of surface ocean pCO2 and pH thermodynamic drivers and the influence on sea-air CO2 flux. *Global Biogeochemical Cycles*, *32*(10), 1476-1497.

Fay, A. R., & McKinley, G. A. (2017). Correlations of surface ocean pco_2 to satellite chloro-

phyll on monthly to interannual timescales. *Global Biogeochemical Cycles, 31*(3), 436-455.

Feely, R. A., Boutin, J., Cosca, C. E., Dandonneau, Y., Etcheto, J., Inouec, H. Y., ... Wanninkhof, R. (2002). Seasonal and interannual variability of CO2 in the equatorial Pacific. *Deep Sea Research Part II: Topical Studies in Oceanography, 49*(13-14), 244-2469.

Feely, R. A., Takahashi, T., Wanninkhof, R., McPhaden, M. J., Cosca, C. E., Sutherland, S. C., & Carr, M. E. (2006). Decadal variability of the air-sea CO2 fluxes in the equatorial Pacific Ocean. *Journal of Geophysical Research: Oceans, 111*(C8), 1-16.

Gallego, M., Timmermann, A., Friedrich, T., & Zeebe, R. E. (2018). Drivers of future seasonal cycle changes in oceanic pCO_2. *Biogeosciences, 15*(17), 5315-5327.

Garcia, H. E., Locarnini, R. A., Boyer, T. P., Antonov, J. I., Baranova, O. K., Zweng, M. M., ... 2014 (2014). *World Ocean Atlas 2013 version 2 (WOA13 V2), Volume 4: Dissolved Inorganic Nutrients (phosphate, nitrate, silicate)* (Tech. Rep.). S. Levitus, Ed.; A. Mishonov, Technical Ed. NOAA Atlas NESDIS 76.

Gorgues, T., Aumont, O., & Rodgers, K. B. (2010). A mechanistic account of increasing seasonal variations in the rate of ocean uptake of anthropogenic carbon. *Biogeosciences, 7*(8), 2581-2589.

Gregg, W. W., & Casey, N. W. (2007). Modeling coccolithophores in the global oceans. *Deep Sea Research Part II: Topical Studies in Oceanography, 54*(5-7), 447-477.

Gregg, W. W., & Conkright, M. E. (2002). Decadal changes in global ocean chlorophyll. *Geophysical Research Letters, 20*(15), 20-1.

Gruber, N., Landschützer, P., & Lovenduski, N. S. (2019). The variable Southern Ocean carbon sink. *Annual Review of Marine Science, 11*, 159-186.

Hauck, J., & Völker, C. (2015). Rising atmospheric CO_2 leads to large impact of biology on Southern Ocean CO_2 uptake via changes of the Revelle factor. *Geophysical research letters, 42*(5), 1459-1464.

Holte, J., Talley, L. D., Gilson, J., & Roemmich, D. (2017). An Argo mixed layer climatology and database. *Geophysical Research Letters, 44*(11), 5618-5626.

Ito, G., Romanou, A., Kiang, N. Y., Faluvegi, G., Aleinov, I., Ruedy, R., ... Lo, K. (2020). Global carbon cycle and climate feedbacks in the NASA GISS ModelE2.1. *Journal of Advances in Modeling Earth Systems.* (in press)

Kelley, M., Schmidt, G., Nazarenko, L., Miller, R., Bauer, S., Ruedy, R., ... Yao, M. (2020). GISS-E2.1: Configurations and Climatology. *Journal of Advances in Modeling Earth Systems, 12*, e2019MS002025.

Key, R. M., Kozyr, A., Sabine, C. L., Lee, K., Wanninkhof, R., Bullister, J. L., ... Peng, T. (2004). A global ocean carbon climatology: Results from Global Data Analysis

Project (GLODAP). *Global Biogeochemical Cycles*, *18*(4), 1-23.

Key, R. M., Tanhua, T., Olsen, A., Hoppema, M., Jutterström, S., Schirnick, C., ... Mintrop, L. (2010). The CARINA data synthesis project: introduction and overview. *Earth System Science Data*, *2*(4), 105-121.

Key, R. M., Tanhua, T., Olsen, A., Hoppema, M., Jutterström, S., Schirnick, C., ... Mintrop, L. (2015). Global Ocean Data Analysis Project, Version 2. *Earth System Science Data*, *2*(4), 105-121.

Landschützer, P., Gruber, N., Bakker, D. C., Stemmler, I., & Six, K. D. (2018). Strengthening seasonal marine CO_2 variations due to increasing atmospheric CO_2. *Nature Climate Change*, *8*(2), 146-150.

Landschützer, P., Gruber, N., Bakker, D. C. E., & Schuster, U. (2014). Recent variability of the global ocean carbon sink. *Global Biogeochemical Cycles*, *29*(9), 927-949.

Landschützer, P., Gruber, N., Bakker, D. C. E., Schuster, U., Nakaoka, S., M, P., ... Zeng, J. (2013). A neural network-based estimate of the seasonal to inter-annual variability of the Atlantic Ocean carbon sink. *Biogeosciences*, *10*, 7793-7815.

Latto, R., & Romanou, A. (2018). The Ocean Carbon States Database: a proof-of-concept application of cluster analysis in the ocean carbon cycle. *Earth System Science Data*, *10*(1), 609-626.

Lauvset, S. K., Key, R. M., Olsen, A., van Heuven, S., Velo, A., Lin, X., ... Watelet, S. (2016). A new global interior ocean mapped climatology: The 1×1 GLODAP version 2. *Earth System Science Data*, *8*, 325-340.

Lefèvre, N., Caniaux, G., Janicot, S., & Gueye, A. K. (2013). Increased CO_2 outgassing in February-May 2010 in the tropical Atlantic following the 2009 Pacific El Niño. *Journal of Geophysical Research: Oceans*, *118*(4), 1645-1657.

Le Quéré, C., Andrew, R. M., Friedlingstein, P., Sitch, S., Hauck, J., Pongratz, J., ... Zheng, B. (2018). Global carbon budget 2018. *Earth System Science Data*, *10*(4), 2141-2194.

Lovenduski, N. S., Gruber, N., Doney, S. C., & Lima, I. D. (2007). Enhanced CO_2 outgassing in the Southern Ocean from a positive phase of the Southern Annular Mode. *Global Biogeochemical Cycles*, *21*(2), 1-14.

Miller, L. A., Chierici, M., Johannessen, T., Noji, T. T., Rey, F., & Skjelvan, I. (1999). An Argo mixed layer climatology and database. *Deep Sea Research Part II: Topical Studies in Oceanography*, *46*(6-7), 1473-1496.

Mogollón, R., & Calil, P. H. (2018). Modelling the mechanisms and drivers of the spatiotemporal variability of pCO_2 and air–sea CO_2 fluxes in the Northern Humboldt Current System. *Ocean Modelling*, *132*, 61-72.

Mongwe, N., Vichi, M., & Monteiro, P. (2018). The seasonal cycle of pCO_2 and CO_2 fluxes in the Southern Ocean: diagnosing anomalies in CMIP5 Earth system models. *Bio-*

geosciences, *15*(9), 2851-2872.

Munhoven, G. (2013). Mathematics of the total alkalinity–pH equation–pathway to robust and universal solution algorithms: the SolveSAPHE package v1.0.1. *Geoscientific Model Development*, *6*(4), 1367-1388.

Najjar, R., & Orr, J. (1999). *Design of ocmip-2 simulations of chlorofluorocarbons, the solubility pump and common biogeochemistry* [OCMIP-2 Protocols]. `http://ocmip5.ipsl.jussieu.fr/OCMIP/`. ([Online; last revised 10-October-1999])

Orr, J. C., Najjar, R. G., Aumont, O., Bopp, L., Bullister, J. L., Danabasoglu, G., ... Yool, A. (2017). Biogeochemical protocols and diagnostics for the CMIP6 Ocean Model Intercomparison Project (OMIP). *Geoscientific Model Development*, *10*, 2169-2199.

Padin, X. A., Vízquez-Rodgríguez, M., Castaño, M., Velo, A., Alonso-Pírez, F., Gago, J., ... Pérez, F. F. (2010). Air-Sea CO_2 fluxes in the Atlantic as measured during boreal spring and autumn. *Biogeosciences*, *7*(5), 1587-1606.

Parard, N., G L a d Lefèvre, & Boutin, J. (2010). Sea water fugacity of CO_2 at the PIRATA mooring at 6° S, 10° W. *Tellus B: Chemical and Physical Meteorology*, *62*(5), 636-648.

Pasquer, B., Metzl, N., Goosse, H., & Lancelot, C. (2015). What drives the seasonality of air–sea CO_2 fluxes in the ice-free zone of the Southern Ocean: A 1D coupled physical–biogeochemical model approach. *Marine chemistry*, *177*, 554-565.

Paulmier, A., Kriest, I., & Oschlies, A. (2009). Stoichiometries of remineralisation and denitrification in global biogeochemical ocean models. *Biogeosciences*, *6*, 923-935.

Pérez García-Pando, C., Miller, R. L., Perlwitz, J. P., Rodríguez, S., & Prospero, J. M. (2016). Predicting the mineral composition of dust aerosols: Insights from elemental composition measured at the Izaña Observatory. *Geophysical Research Letters*, *43*(19), 10520-10529.

Perlwitz, J. P., & Pérez García-Pando, R. L., Miller. (2015). Predicting the mineral composition of dust aerosols Part 1: Representing key processes. *Atmospheric Chemistry Physics*, *15*, 11593-11627.

Perlwitz, J. P., Pérez García-Pando, C., & Miller, R. L. (2015). Predicting the mineral composition of dust aerosols — Part 2: Model evaluation and identification of key processes with observations. *Atmospheric Chemistry Physics*, *15*, 11629-11652.

Riebesell, U., Körtzinger, A., & Oschlies, A. (2009). Sensitivities of marine carbon fluxes to ocean change. *Proceedings of the National Academy of Sciences*, *106*(49), 20602-20609.

Rodgers, K. B., Sarmiento, J. L., Aumont, O., Crevoisier, C., de Boyer Montégut, C., & Metzl, N. (2008). A wintertime uptake window for anthropogenic CO2 in the North Pacific. *Global Biogeochemical Cycles*, *22*(2), 1-16.

Roemmich, D., & Gilson, J. (2009). The 2004–2008 mean and annual cycle of tempera-

ture, salinity, and steric height in the global ocean from the Argo Program. *Progress in oceanography*, *82*(2), 81-100.

Romanou, A., Gregg, W. W., Romanski, J., Kelley, M. R., Bleck, Healy, R., Nazarenko, L., ... Tausnev, N. (2013). Natural air–sea flux of CO_2 in simulations of the NASA-GISS climate model: sensitivity to the physical ocean model formulation. *Ocean Modelling*, *66*, 26-44.

Romanou, A., Marshall, J., Kelley, M., & Scott, J. (2017). Role of the ocean's AMOC in setting the uptake efficiency of transient tracers. *Geophysical research letters*, *44*(11), 5590-5598.

Romanou, A., Romanski, J., & Gregg, W. W. (2014). Natural ocean carbon cycle sensitivity to parameterizations of the recycling in a climate model. *Biogeosciences*, *11*(4), 1137-1154.

Sarmiento, J. L., & Gruber, N. (2006). *Ocean Biogeochemical Dyanmics*. Princeton, NJ: Princeton University Press.

Schmidt, G. A., Kelley, A., Nazarenko, L., Ruedy, R., L, R. G., Bauer, I. A. M., ... Zhang, J. (2014). Configuration and assessment of the GISS ModelE2 contributions to the CMIP5 archive. *Journal of Advances in Modeling Earth Systems*, *6*(1), 141-184.

Sutton, A. J., Feely, R. A., Sabine, C. L., McPhaden, M. J., Takahashi, T., Chavez, F. P., ... Mathis, J. T. (2014). Natural variability and anthropogenic change in equatorial Pacific surface ocean pCO_2 and pH. *Global Biogeochemical Cycles*, *28*(2), 131-145.

Takahashi, T., Olafsson, J., Goddard, J. G., Chipman, D. W., & Sutherland, S. C. (1993). Seasonal variation of CO2 and nutrients in the high-latitude surface oceans: A comparative study. *Global Biogeochemical Cycles*, *7*(4), 843-878.

Takahashi, T., Sutherland, S., Wanninkhof, R., Sweeney, C., Feely, R., Chipman, D. W., ... de Baar, H. J. W. (2009). Climatological mean and decadal change in surface ocean pCO_2, and net sea–air CO_2 flux over the global oceans. *Deep Sea Research Part II: Topical Studes in Oceanography*, *56*(8-10), 554-577.

Takahashi, T., Sutherland, S. C., Chipman, D. W., Goddard, J. G., Ho, C., Newberger, T., ... Munro, D. R. (2014). Climatological distributions of pH, pCO_2, total CO_2, alkalinity, and $CaCO_3$ saturation in the global surface ocean, and temporal changes at selected locations. *Marine Chemistry*, *164*, 95-125.

Takahashi, T., Sutherland, S. C., Sweeney, C., Poisson, A., Metzl, N., Tilbrook, B., ... Nojiri, Y. (2002). Global sea–air CO_2 flux based on climatological surface ocean pCO_2, and seasonal biological and temperature effects. *Deep Sea Research Part II: Topical Studies in Oceanography*, *49*(9-10), 1601-1622.

Valsala, V. K., Roxy, M. K., Ashok, K., & Murtugudde, R. (2014). Spatiotemporal characteristics of seasonal to multidecadal variability of pCO_2 and air-sea CO_2 fluxes in

1452 the equatorial Pacific Ocean. *Journal of Geophysical Research: Oceans*, *119*(12),
1453 8987-9012.
1454 Wang, X., Murtugudde, R., Hackert, E., Wang, J., & Beauchamp, J. (2015). Seasonal to
1455 decadal variations of sea surface pCO_2 and sea-air CO_2 flux in the equatorial oceans
1456 over 1984–2013: A basin-scale comparison of the Pacific and Atlantic Oceans. *Global*
1457 *Biogeochemical Cycles*, *29*(5), 597-609.
1458 Westberry, T., Behrenfeld, M. J., Siegel, D. A., & Boss, E. (2008). Carbon-based primary pro-
1459 ductivity modeling with vertically resolved photoacclimation. *Global Biogeochemi-*
1460 *cal Cycles*, *22*(2), 1-18.